031307-9-T

FAST FINITE ELEMENT-BOUNDARY INTEGRAL IMPLEMENTATION FOR SLOT ANTENNA ANALYSIS USING THE AIM ALGORITHM

Sunil Bindiganavale
John L. Volakis

July 1997

31307-9-T = RL-2445

Theory and code manual for AIM-Plate and AIM-Prism

Sunil S. Bindiganavale and John L. Volakis

Radiation Laboratory
Department of Electrical Engineering and Computer Science
The University of Michigan
Ann Arbor, MI 48109-2122

This report describes the theory and execution procedure for AIM-Plate and AIM-Prism. AIM-Plate performs the same functions as a standard moment method code for analysis of planar conducting scatterers but with drastically reduced memory requirement and solution time. This reduction is accomplished by incorporating the Adaptive Integral Method (AIM) in an iterative solution of the Electric Field Integral Equation (EFIE). AIM-Prism performs the same functions as a Finite Element-Boundary Integral (FE-BI) program for radiation and scattering analysis from planar cavity-backed antennas. However, incorporation of AIM in boundary integral computations alleviates memory and execution time requirements considerably thus enabling the analysis of antenna configurations which result in large numerical systems.

1 Working principle of AIM-Plate

A metallic scatterer can be considered as a special case of a resistive body with the resistivity $R_r = 0$. A resistive body is modeled using the resistive boundary condition [1]

$$\hat{n} \times (\mathbf{E}^i + \mathbf{E}^s) = \eta_0 R_r \mathbf{J} \tag{1}$$

Consider a resistive body illuminated by an incident plane wave of unit amplitude given by

$$\mathbf{E}^i = (\hat{\theta}\cos\alpha + \hat{\phi}\sin\alpha)\, e^{jk_o(x\sin\theta_i\cos\phi_i + y\sin\theta_i\sin\phi_i)} \tag{2}$$

where k_0 is the free space wavenumber, α is the polarization angle and (θ_i, ϕ_i) indicate the direction of incidence. The scattered field $\mathbf{E}^s$ can be determined from the surface current $\mathbf{J}$ according to

$$\mathbf{E}^s = -j\omega\mathbf{A} - \nabla\phi \tag{3}$$

where the magnetic vector potential $\mathbf{A}$ is given by

$$\mathbf{A}(\mathbf{r}) = \frac{\mu_o}{4\pi}\iint_S \mathbf{J}(\mathbf{r}')\frac{e^{-jk_oR}}{R}\,dS' \tag{4}$$

with S being the surface of the body. The scalar potential ϕ is given by

$$\phi(\mathbf{r}) = \frac{1}{4\pi\epsilon_o} \iint_S \sigma(\mathbf{r}') \frac{e^{-jk_oR}}{R} dS'. \tag{5}$$

where R is the distance between observation and source points, viz.

$$R = |\mathbf{r} - \mathbf{r}'| = \sqrt{(x-x')^2 + (y-y')^2 + (z-z')^2} \tag{6}$$

The continuity equation is used to relate the surface charge density and the current

$$\nabla_s \cdot \mathbf{J} = -j\omega\sigma \tag{7}$$

Enforcing (1) on S yields the electric field integral equation for $\mathbf{J}$

$$\mathbf{E}^i_{tan} = (j\omega\mathbf{A} + \nabla\phi)_{tan} + \eta_o R_r \, \mathbf{J} \quad \mathbf{r} \in S \tag{8}$$

To model the current, the scatterer is discretized into triangular patches. The current is then expanded in terms of vector basis functions [2] which are especially suited for triangular domains. Each basis function is associated with an interior (nonboundary) edge, and is nonzero only on the two triangles sharing that edge. Figure 1 shows the n^{th} interior edge shared by triangles T_n^+ and T_n^- of area A_n^+ and A_n^- respectively. A point in the triangle pair

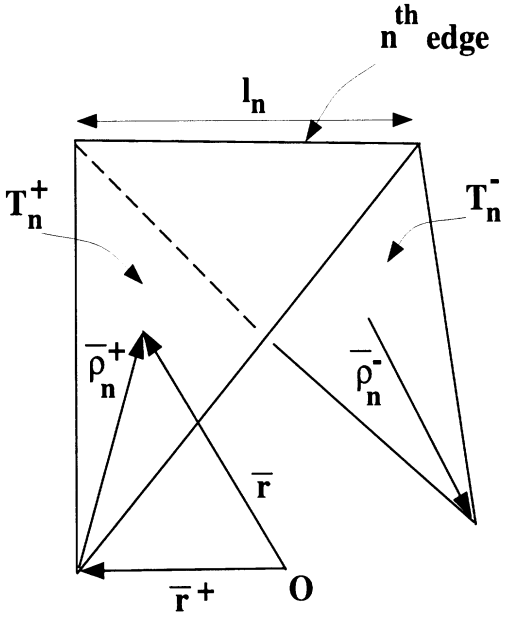

Figure 1: Local coordinates for the n^{th} edge

can be designated by either the global position vector $\mathbf{r}$, or local position vectors $\overline{\rho_n}^{\pm} = \mathbf{r} - \mathbf{r}_n^{\pm}$. The basis function $\mathbf{f}_n(\mathbf{r})$ for the n^{th} edge is defined as

$$\mathbf{f}_n(\mathbf{r}) = \begin{cases} \frac{l_n}{2A_n^+}\overline{\rho_n^+}, & \mathbf{r} \ in \ T_n^+ \\ \frac{l_n}{2A_n^-}\overline{\rho_n^-}, & \mathbf{r} \ in \ T_n^- \\ 0, & \text{otherwise} \end{cases} \tag{9}$$

The current $\mathbf{J}$ on S is approximated by

$$\mathbf{J} \cong \sum_{n=1}^{N} I_n \mathbf{f}_n(\mathbf{r}) \tag{10}$$

where N is the number of interior edges and the unknown coefficients I_n represents the current density flowing across the n^{th} edge of the mesh shared by the T_n^+ and T_n^- triangles. To solve for the basis coefficients, Galerkin's technique is applied to (8) giving

$$\iint_S \mathbf{E}_i \cdot \mathbf{f}_m \, dS = j\omega \iint_S \mathbf{A} \cdot \mathbf{f}_m \, dS - \iint_S \phi \nabla_s \cdot \mathbf{f}_m \, dS + \eta_o \iint_S R_r \mathbf{J} \cdot \mathbf{f}_m \, dS \; m = 1, ..., N. \quad (11)$$

Using (9) in (11) yields the $N \times N$ system of linear equations, $V = ZI$ where I_n is the N^{th} basis coefficient, Z_{mn} is the impedance matrix whose elements are computed from

$$\begin{aligned} Z_{mn} &= \frac{\eta_o l_m l_n}{4} \left\{ \frac{j}{2} \iint_{T_m^\pm} \iint_{T_n^\pm} \frac{1}{A_m^\pm A_n^\pm} \rho_m^\pm(\mathbf{r}) \cdot \rho_n^\pm(\mathbf{r}') \frac{e^{-jk_oR}}{R} \, dS'dS \right. \\ &- \frac{j}{2\pi^2} \iint_{T_m^\pm} \iint_{T_n^\pm} \frac{\epsilon_m \epsilon_n}{A_m^\pm A_n^\pm} \frac{e^{-jk_oR}}{R} \, dS'dS \\ &+ \left. \iint_{T_m^\pm} \frac{R_n^\pm}{A_m^\pm A_n^\pm} \rho_m^\pm(\mathbf{r}) \cdot \rho_n^\pm(\mathbf{r}) \, dS \right\} \end{aligned} \quad (12)$$

where ϵ_m and ϵ_n are the positive current reference signs for edges m and n, defined as

$$\epsilon_m = \begin{cases} +1 & \mathbf{r} \; in \; T_m^+ \\ -1 & \mathbf{r} \; in \; T_m^- \end{cases} \quad (13)$$

and

$$\epsilon_n = \begin{cases} +1 & \mathbf{r}' \; in \; T_n^+ \\ -1 & \mathbf{r}' \; in \; T_n^- \end{cases} \quad (14)$$

The elements of the interaction matrix can be computed directly from (12). However, a more convenient way of evaluating these elements is to consider a pair of faces and compute all nine interactions between edges contained by this pair. This enables the loops for assembly of the matrix elements to be over faces, instead of edges, thus speeding up the assembly process. For an observation face p paired with a source face q, the quantity Z_{mn}^{pq} is computed for all mn edge pairs as

$$\begin{aligned} Z_{mn}^{pq} &= \frac{\eta_o l_m l_n \epsilon_m^p \epsilon_n^q}{4A^pA^q} \left[\frac{j}{2} \iint_{T_p} \iint_{T_q} \rho_m^+(\mathbf{r}) \cdot \rho_n^+(\mathbf{r}') \frac{e^{-jk_oR}}{R} \, dS'dS \right. \\ &- \frac{j}{2\pi^2} \iint_{T_p} \iint_{T_q} \frac{e^{-jk_oR}}{R} \, dS'dS \\ &+ \left. R_r^q \iint_{T_q} \rho_m^+(\mathbf{r}) \cdot \rho_n^+(\mathbf{r}) \, dS \right\} \end{aligned} \quad (15)$$

The positive current reference signs, ϵ_m and ϵ_n, are now assigned according to

$$\epsilon_m^p = \begin{cases} +1, & if \; T^p \; is \; T_m^+ \\ -1, & if \; T^p \; is \; T_m^- \end{cases} \quad (16)$$

and

$$\epsilon_n^q = \begin{cases} +1, & if \; T^q \; is \; T_n^+ \\ -1, & if \; T^q \; is \; T_n^- \end{cases} \quad (17)$$

The integrals in (15) are evaluated for near and self cells by the techniques detailed in [3]. It should be noted that in (15) $T_p = T_p^+ + T_p^-$ and $T_q = T_q^+ + T_q^-$, thus computation of Z_{mn}^{pq} involves summation over four triangles. The elements of the excitation vector are given by

$$V_m = \frac{l_m}{2} \int_{T_m^\pm} \frac{\rho_m^\pm(\mathbf{r})}{A_m^\pm} \cdot (\hat{\theta} \cos\alpha + \hat{\phi} \sin\alpha) \; e^{jk_o(x \sin\theta_i \cos\phi_i + y \sin\theta_i \sin\phi_i)} \, dS. \tag{18}$$

The $N \times N$ linear system can be solved either by direct methods such as matrix factorization (which would mean an execution time of $O(N^3)$) or iterative methods involving an operation count of $O(N^2)$/iteration.

The Adaptive Integral Method is an algorithm which reduces the computationally complexity of moment method solutions. In the case of AIM, the CPU reduction is achieved by mapping the original MM discretization onto a rectangular grid and exploiting the Toeplitz property of the Green's function on this grid. That is, the Fast Fourier Transform (FFT) is invoked to compute the matrix-vector products in the iterative solver. For an arbitrary three dimensional body, a three dimensional FFT is required and as can be understood, this calculation is very time consuming. For planar scatterers the dimensionality of the FFT is reduced by one, thereby significantly accelerating the solution. In this report, we examine the benefits of AIM when the body is not electrically large, but is highly tessellated owing to its intricate construction, thus leading to a large unknown count. We show that significant savings in CPU and memory can be achieved by AIM and examine its accuracy for near field and far field computations.

1.1 AIM for Planar Scatterers

In this report, we describe the application of AIM to planar scatterers. Following the standard moment method discretization procedure, we begin with the linear system

$$[Z]\{I\} = \{V\} \tag{19}$$

with $[Z]$ being the elements interaction matrix, whereas $\{I\}$ is the vector of the unknown coefficients and $\{V\}$ is the excitation vector. The matrix $[Z]$ is fully populated, demanding $O(N^2)$ storage, and each $[Z]\{I\}$ matrix-vector product requires $O(N^2)$ multiplications.

Fast algorithms such as FMM and AIM are used to reduce the operation count from N^2 down to N^α, where $\alpha \leq 1.5$. Both algorithms work on approximating the far zone interactions. In the case of AIM, the CPU reduction is achieved by first splitting the matrix as

$$[Z] = [Z^{near}] + [Z^{far}] \tag{20}$$

based on a threshold distance referred to as the near-zone radius. The matrix $[Z^{near}]$ contains the interactions between elements separated less than the threshold distance, whereas $[Z^{far}]$ contains the remaining interactions. The elements of $[Z^{near}]$ are evaluated with the exact MM while those of $[Z^{far}]$ and the product $[Z^{far}]\{I\}$ are evaluated in an approximate manner as prescribed by the AIM procedure [4].

Application of AIM requires that the whole geometry be enclosed in a regular rectangular grid. Basically, the fields of each interior edge is re-expressed using a new expansion based

on delta sources located at the nodes of the uniform AIM grid as depicted in Figure 2. For the m^{th} edge, this new expansion has the form

$$\overline{\psi}_m = \sum_{q=1}^{M^2} \delta(x - x_{mq})\delta(y - y_{mq})[\Lambda^x_{mq}\hat{x} + \Lambda^y_{mq}\hat{y}] \tag{21}$$

where $\mathbf{r}_{mq}$ are the position vectors of M^2 points on the square surrounding the center of the edge and $\delta(x)$ is the usual Dirac delta function. The coefficients $\Lambda^{x,y}_m$ are suitably chosen so that the new expansion is equivalent to the original representation using triangular elements. A similar expansion is used for the divergence of the basis functions

$$\psi^d_m = \sum_{q=1}^{M^2} \delta(x - x_{mq})\delta(y - y_{mq})\Lambda^d_{mq} \tag{22}$$

To find a relation between the $\Lambda^{x,y}_m$ and I_n coefficients, we equate moments of the two expansions up to order M. Specifically, we set

$$\mathbf{M}^m_{q_1,q_2} = \mathbf{F}^m_{q_1,q_2} \tag{23}$$

where

$$\begin{aligned} \mathbf{M}^m_{q_1 q_2} &= \int_{-\infty}^{\infty}\int_{-\infty}^{\infty} \overline{\psi}_m (x - x_a)^{q_1}(y - y_a)^{q_2} dxdy \quad for \;\; 0 \le q_1, q_2 \le M \\ &= \sum_{q=1}^{M^2} (x_{mq} - x_a)^{q_1}(y_{mq} - y_a)^{q_2}[\Lambda^x_{mq}\hat{x} + \Lambda^y_{mq}\hat{y}] \;\; with \;\; q = q_1 + q_2 \end{aligned} \tag{24}$$

$$\mathbf{F}^m_{q_1 q_2} = \int_{-\infty}^{\infty}\int_{-\infty}^{\infty} \mathbf{f}_m (x - x_a)^{q_1}(y - y_a)^{q_2} dxdy \tag{25}$$

Similarly, by equating moments of $\nabla_s \cdot \mathbf{J}_s$ with the new expansion (22), we establish a relation between Λ^d_m and I_n. That is, we set

$$D^m_{q1,q2} = H^m_{q1,q2} \tag{26}$$

where

$$D^m_{q_1 q_2} = \int_{-\infty}^{\infty}\int_{-\infty}^{\infty} \psi^d_m (x - x_a)^{q_1}(y - y_a)^{q_2} dxdy = \sum_{q=1}^{M^2} (x_{mq} - x_a)^{q_1}(y_{mq} - y_a)^{q_2}\Lambda^d_{mq} \tag{27}$$

$$H^m_{q_1 q_2} = \int_{-\infty}^{\infty}\int_{-\infty}^{\infty} \nabla_s \cdot \mathbf{f}_m (x - x_a)^{q_1}(y - y_a)^{q_2} dxdy \tag{28}$$

(23) and (26) give three $M^2 \times M^2$ systems yielding the equivalence coefficients as the solution. This process is depicted pictorially in Figure 2.

Were we to use the equivalent expansions to represent the currents everywhere, the resulting impedance matrix will be of the form

$$[Z]^{total}_{AIM} = \sum_{i=1}^{3} [\Lambda]_i [G] [\Lambda]^T_i \tag{29}$$

In this, $[\Lambda]_i$ are the sparse matrices containing the coefficients of the expansion (21) and (22) whereas $[G]$ is the Toeplitz matrix whose elements are the free space Green's function

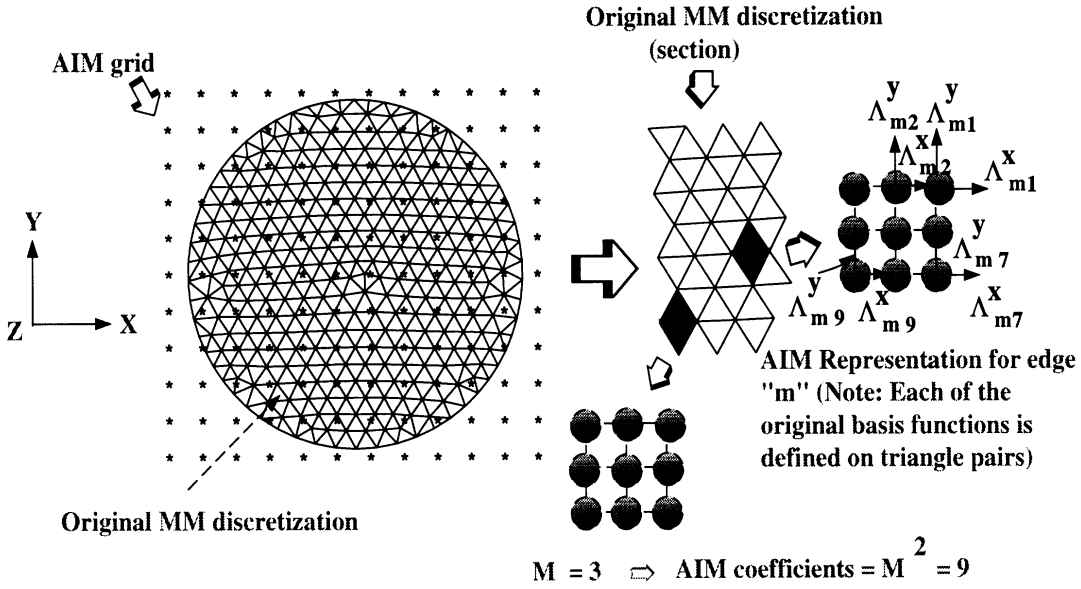

Figure 2: The process of transformation from the original MM grid onto the AIM grid

evaluated at the grid points. It has been shown in [4] that $[Z_{AIM}^{total}]$ is not of sufficient accuracy for modeling the interactions between the nearby current elements. To take advantage of the Toeplitz structure of $[G]$ and sparsity of $[\Lambda]$ we can still use $[Z_{AIM}^{total}]$ to represent the far element interactions. However, we will retain the exact interaction matrix elements for the near element interactions. That is, we rewrite $[Z_{AIM}^{total}]$ as

$$[Z]_{AIM}^{total} = [Z]_{AIM}^{near} + [Z]_{AIM}^{far} \tag{30}$$

Comparing this to (20) and setting $[Z]^{far} \simeq [Z]_{AIM}^{far}$ we can rewrite the original $[Z]$ matrix as

$$[Z] \simeq ([Z]^{near} - [Z]_{AIM}^{near}) + [Z]_{AIM}^{total} \tag{31}$$

or

$$[Z] \simeq [S] + \sum_{i=1}^{3} [\Lambda]_i [G] [\Lambda]_i^T \tag{32}$$

where $[S] = [Z]^{near} - [Z]_{AIM}^{near}$ is a sparse matrix corresponding to the difference between the near field interactions computed by MM and AIM. The Toeplitz property of the Green's function, defined on the regular grid, enables use of the FFT to accelerate the computation of the matrix-vector product. The sequence of operations involved in the construction of the coefficient and Green's function matrices are indicated in Figure 3(a); those for the matrix-vector product execution are outlined in Figure 3(b). In the computation of the matrix-vector product, the initial step of transforming the currents from the original MM grid onto the uniform AIM grid is comparable to the grouping operation of the FMM. While the FMM relies on grouping to reduce the number of scattering centers, the sequence of operations in AIM can be interpreted as a realignment of scattering centers onto a regular grid. Although, this process does not reduce the number of scattering centers, the regularity of their location enables use of the FFT for fast computation of matrix-vector products.

1.2 Results

When examining the merits of a fast integral algorithm such as AIM, of importance is the memory and CPU requirements, both contrasted to the delivered accuracy. Although

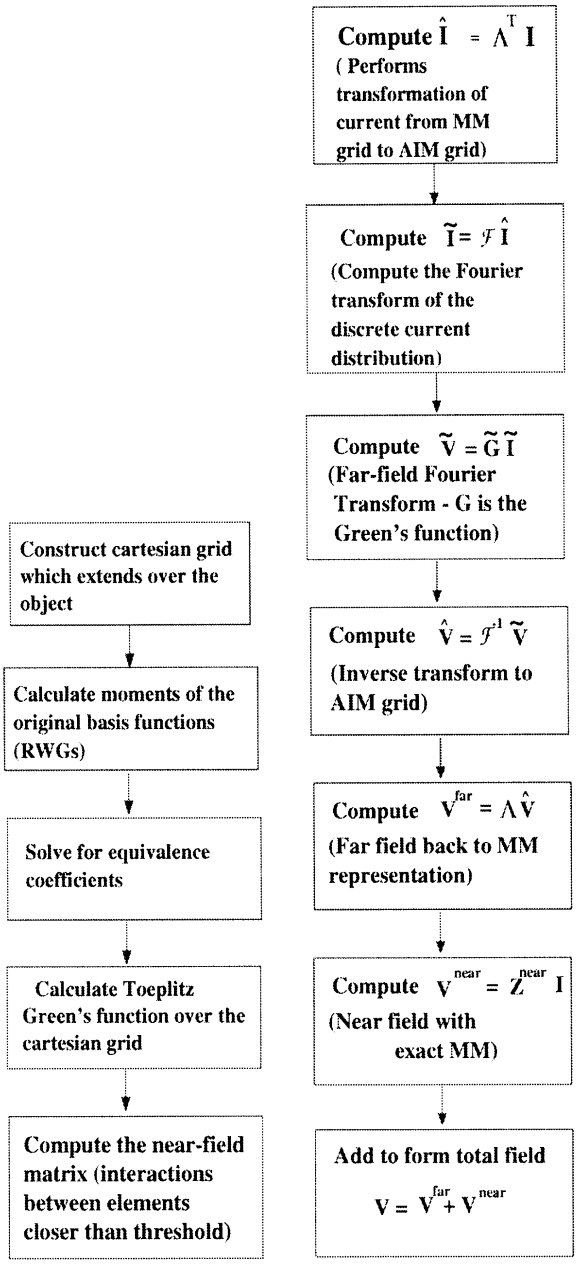

Figure 3: (a) Matrix build operations and (b) Matrix vector product computation in AIM

approximate analytical expressions have been derived in [4] for some of these parameters, these refer to implementations involving cubical grids and the three-dimensional FFT. Our goal in this chapter is to assess the accuracy of AIM in treating small details within an aperture/surface and to provide the reader with quantitative measures on the performance of AIM when implemented with the two dimensional FFT. The near-zone radius or threshold distance has a dramatic impact on the CPU requirements since it controls the non-zero element population of the system matrix. In the case of AIM, because of the inherent mapping to a uniform grid, we are highly interested in examining its suitability to model small and fine details embedded in much larger scale structures. The calculations for the plate configurations given next are intended to address this issue by examining the method's

performance for a number of representative and practical situations. All of the included results were generated using single precision arithmetic on an HP9000/C-110 workstation with a rated peak speed of 47 Mflops (the level 4 optimization option was also used). In all cases, a third order (M=3) multipole expansion was used with a grid spacing of 0.05λ.

Figures 4-8 depict the $\hat{\theta}\hat{\theta}$ and $\hat{\phi}\hat{\phi}$ polarization radar cross section patterns ($\phi = 0^0$ cut) as calculated by AIM for the different threshold distances indicated on the figures. The first circular plate has no holes and was used to validate the method. From the pattern comparisons, it is clear that AIM recovers the exact result very well. As given in Table 1 and 2, AIM achieves this with at least a factor of five less memory thanthe traditional MM, even though the geometries are still rather small to demonstrate the full impact of AIM. Also, Table 2 shows that a near zone radius of 0.3λ is sufficient to maintain good accuracy (below one dB in RMS error [5]).

The advantage of AIM is more pronounced when gaps are inserted into the plate's surfaces and this is the primary reason that one may prefer AIM over other fast integral methods for planar structures. As depicted in Figures 5 and 6, AIM maintains its accuracy for the same threshold criterion even though the gaps/slots have a dominant effect on the RCS pattern as shown in Figure 5. In the case of narrow slots (or thin ridges in the plates) of width 0.03λ, the memory requirements of the traditional MM increase quickly due to the higher element density. For the geometry in Figure 7, AIM yields memory saving of 79% and the CPU time is reduced by a factor of 12 while retaining the monostatic pattern accuracy to within a tenth of a dB. This is achieved by using a uniform AIM grid density of 20 points per linear wavelength even though the cell density of the original plate mesh is much greater due to the narrow slot. One may assume that this change in grid density will affect the near zone field. However, our observations indicate that the surface current is equally accurate. For the configuration in Figure 7 the average current density error is 7.3% for a threshold distance of 0.2λ and 6% for a threshold distance of 0.4λ. The currents for the geometry in Figure 7 along the center narrow strip are plotted and compared in Figure 9. These results demonstrate the important feature that the near zone threshold criterion is not affected by the specific geometrical details, leading to tremendous memory savings. Moreover, the accuracy of the results provide a convincing argument that AIM can efficiently handle highly irregular and resonant (i.e. antenna) geometries as well as smooth scatterers. At the same time, the convergence rate of the AIM system is unaffected indicating that the system condition is unchanged. This is of critical importance for fast iterative solutions, since an increase in the iteration count would annul the faster computation of the matrix-vector product.

Figure 8 shows the monostatic RCS pattern for a grating structure which acts as a "polarization filter". The thin ridges in the grating cause a strong specular return for the $\hat{\phi}\hat{\phi}$ polarization (almost 10 dB above the return in the absence of the gratings) as is evident from the results in Figure 8(d). Of importance is that the MM triangular mesh in Figure 8 required a cell size of 0.02λ per linear dimension because of the narrow grating. However, the overlaid rectangular AIM grid could be selected to have a much coarser discretization. More specifically, we chose grid spacings of 0.05λ and 0.1λ for the AIM grid and, thus, computational requirements of AIM were much lower. For the 0.1λ grid spacing the solution time was reduced from 2.75 minutes down to only 12 secs at the expense of some accuracy (fraction of a dB). To further increase in accuracy, we employed a 0.05λ grid spacing and as shown in Figure 8(b) the AIM curve is now indistinguishable from the reference MM result (within 0.1 dB). From Tables 1 and 2, the AIM computational and memory requirements are 8 times and 9 times less, respectively, without loss of accuracy. This is a significant

observation and we have found that both the convergence rate and condition of the AIM system remains essentially unchanged from the original moment method system. The original discretization for the geometry in Figure 8 and the equivalent AIM grids are pictorially depicted in Figure 10. It should be noted that even though the size of the discretization is very small, retaining the self-cell term alone in the moment method system introduces huge error (Figure 11), thus emphasizing the importance of non-self terms.

1.3 Summary

The performance of AIM is much improved when applied to scattering from flat complex scatterers and scatterers with high discretization rates. Thus, the reduction of solution time is considerably more for the geometries depicted in Figure 12(a) and 13(a) than for the geometries in Figure 12(b) and 13(b). A memory reduction of 5 to 10 times over traditional MM was observed without compromise in accuracy when using a threshold radius of 0.2λ. This CPU reduction is achieved without resorting to parallelization or optimization techniques (as is known AIM is particularly amenable to such improvements). More importantly, the AIM algorithm is capable of modeling very small details in large bodies with a high degree of accuracy, while simultaneously saving considerable memory. This is of importance when modeling broadband antennas (spirals or log-periodics) and gratings which are both large in overall size but can contain features as small as $\lambda/100$ in size. Application of AIM for analysis of cavity-backed antennas is described in the next section.

Geometry	Discretization			MM memory (MB)	MM solution time $\hat{\theta}\hat{\theta}$ pol ($\theta = 0^0$ inc.)
	Facets	Edges	Unknowns		
Figure 4	586	908	850	5.51	32 secs
Figure 5	554	890	772	4.54	29 secs
Figure 6	1130	1806	1584	19.14	4 mins 50 secs
Figure 7	1036	1667	1441	15.84	4 mins
Figure 8	1038	1957	1157	10.21	2 mins 45 secs

Table 1: Solution CPU time and memory requirement of the moment method

1.4 AIM-Plate execution

The execution of AIM-Plate is done in a three step process

1. Convert the meshed geometry file from IDEAS Master Series 2.1 into a format required by the code. This is done with the help of two mesh-processing programs - `ms21_u2c.f` and `c2p_fast.f` and the transcript of a session with these programs with reference to the geometry of Figure 8 is indicated below

```
[ 271 ] PlateFreqAIM.dir -: ms21_u2c
 Name of universal file ?
Pl118slotss025.unv
```

Geometry	AIM Data					
	Threshold (λ)	Non-Zeros in Near Z	Memory (MB)	Solution time $\hat{\theta}\hat{\theta}$ pol ($\theta = 0^0$ inc.)	RMS Error(dB) $\hat{\theta}\hat{\theta}$ pol	$\hat{\phi}\hat{\phi}$ pol
Figure 4	0.3	59928	0.68	23 secs	0.1718	0.0755
	0.4	100182	1.14	25 secs	0.1490	0.0693
	0.7	257390	2.94	28 secs	0.0728	0.0490
Figure 5	0.4	79030	0.9	21 secs	0.0728	0.0583
	0.6	157994	1.8	27 secs	0.0721	0.0520
Figure 6	0.7	283774	3.24	3 mins 32 secs	0.8017	0.5185
Figure 7	0.2	296250	3.39	20 secs	0.1063	0.0949
	0.4	649556	7.43	31 secs	0.0548	0.0632
Figure 8	0.2	120220	1.37	18 secs	0.0469	0.0469

Table 2: Solution CPU time, memory requirement and RMS error of AIM (all entries in this table were computed with an AIM grid spacing of 0.05λ)

```
 Name of converter file ?
cnv
 Encountered header
 There are  912 nodes.
 There are  1038 elements.
[ 273 ] PlateFreqAIM.dir -: c2p_fast
 Name of data file?
Pl118slotss025Dat
 Finished reading in data
 There are  912 nodes
 There are  1038 elements
 Be patient #*!?/#@*!!!
 100 elements done
 200 elements done
 300 elements done
 400 elements done
 500 elements done
 600 elements done
 700 elements done
 800 elements done
 900 elements done
 1000 elements done
 Max. no. of edges emanating from a node =  6
 1957 1957
 Edge count =  1957
 Finding free edges
 There are  800 free edges
```

2. Run the AIM preprocessor program to determine the appropriate dimensions to be set in the file `dim.inc`. The transcript of a session with `PreProc.f` is indicated below

again with reference to the geometry of Figure 8

```
[ 262 ] PlateFreqAIM.dir -: PreProc
 Input name of mesh file (Note: Dimensions
 are assumed to be in CENTIMETER) !
Pl1l8slotss025Dat
 maxx= .5
 minx= -.5
 maxy= .5
 miny= -.5

 Input frequency at which the structure will be
 analyzed (GHz)
30

 Enter AIM grid step in WAVELENGTHS (0.05 suggested)
 Note: The main AIM code has been hard-wired for
 0.05 lambda but can be easily changed to 0.1 lambda
 by changing the variable step
.05

 nx in main progam to be=  25
 ny in main progam to be=  25
 FFT order along x (iFFTx in main pgm) 64
 FFT order along y (iFFTy in main pgm) 64
 Total number of elements= 1957
 maxnod= 2700
 maxedg= 8100
 maxtri= 5400
 nmax= 4
 nintedg= 1157
 ntris= 1038

 Order of system =  1157
 No. of triangular elements =  1038


 Enter near field threshold in CENTIMETER
 Note: This is related to the Maximum
 number of non-zeros in the near-field matrix
 Recommend this to be 0.2-0.7 times the
 wavelength in centimeter. This is a
 empirical quantity and needs to be
 determined by trial & error
0.2
 Set number of nonzeros in Near Z = 60110
```

3. Now the AIM program is executed and a sample session is indicated below

```
[ 259 ] PlateFreqAIM.dir -: FltrcAIM
 Enter mesh file name:
Pl1l8slotss025Dat
 Enter surface type (1-pec):
1
 Enter output file name:
Opfile
 Enter pattern (1-bistatic, 2-backscatter):
2
 Enter E-field polarization angle alpha (in degrees):
0
 Number of cuts
1
 Enter cut specifications...
 Fix (1-phi, 2-theta):
1
 Enter fixed observation angle phi (in degrees):
0
 Enter start observation angle theta (in degrees):
0
 Enter stop observation angle theta (in degrees):
90
 Enter number of observation points:
91
 Enter Frequency (GHz)
30

 --------------- Files ---------------
            Mesh:  Pl1l8slotss025Dat
          Output:  Opfile

 ------------ Surface Type -----------
                  PEC

 ------------ Pattern Type -----------
              Backscatter


 -------- Observation Angles ---------
 Number of cuts  : 1
   Cut # 1
 -----------
            Phi:      .00 deg.
    Start Theta:      .00 deg.
     Stop Theta:    90.00 deg.

 --- Number of Observation Points ----
```

```
                91

 ---Frequency of analysis:   30.0  GHz--

 Above data O.K. (1-Yes, 2-No)?
1
 Finished reading nodes
 Finished reading elements
 Interior edges =  1157
 No. of triangular facets =  1038
 50 triangles done
 100 triangles done
 150 triangles done
 200 triangles done
 250 triangles done
 300 triangles done
 350 triangles done
 400 triangles done
 450 triangles done
 500 triangles done
 550 triangles done
 600 triangles done
 650 triangles done
 700 triangles done
 750 triangles done
 800 triangles done
 850 triangles done
 900 triangles done
 950 triangles done
 1000 triangles done
 Equivalence coefficients computed now
 50 elements done
 100 elements done
 150 elements done
 200 elements done
 250 elements done
 300 elements done
 350 elements done
 400 elements done
 450 elements done
 500 elements done
 550 elements done
 600 elements done
 650 elements done
 700 elements done
 750 elements done
 800 elements done
```

```
 850 elements done
 900 elements done
 950 elements done
 1000 elements done
 1050 elements done
 1100 elements done
 1150 elements done
 Toeplitz G calculation


 Enter near field threshold in CENTIMETER
 Note: This is related to the Maximum
 number of non-zeros in the matrix
 Recommend this to be 0.2-0.7 times the
 wavelength in centimeter. This is a
 empirical quantity and needs to be
 determined by trial & error
0.2
```

The output will then appear in the following format indicating the angles of observation (Phi & Theta), Backscatter RCS and number of BCG iterations for convergence.

Phi	Theta	Alpha=0	BCG Iter
0.00	0.00	0.074222	484
0.00	1.00	0.068417	148
0.00	2.00	0.047878	168
0.00	3.00	0.013304	161
0.00	4.00	-0.036448	161
0.00	5.00	-0.097169	161
0.00	6.00	-0.171789	171
0.00	7.00	-0.258932	185
0.00	8.00	-0.356277	178
0.00	9.00	-0.463876	172
0.00	10.00	-0.581200	191
0.00	11.00	-0.704883	194
0.00	12.00	-0.832557	179
0.00	13.00	-0.972245	203
0.00	14.00	-1.111443	198
0.00	15.00	-1.254094	184
0.00	16.00	-1.397070	189
0.00	17.00	-1.541648	177
0.00	18.00	-1.684258	141
0.00	19.00	-1.823769	140
0.00	20.00	-1.961649	142
0.00	21.00	-2.096322	146

0.00	22.00	-2.226939	147
0.00	23.00	-2.354322	149
0.00	24.00	-2.481832	177
0.00	25.00	-2.606813	156
0.00	26.00	-2.730812	148
0.00	27.00	-2.855004	147
0.00	28.00	-2.980468	146
0.00	29.00	-3.109120	148
0.00	30.00	-3.241405	148
0.00	31.00	-3.379283	147
0.00	32.00	-3.521605	171
0.00	33.00	-3.672821	172
0.00	34.00	-3.834239	189
0.00	35.00	-4.003928	167
0.00	36.00	-4.180166	132
0.00	37.00	-4.379130	180
0.00	38.00	-4.581637	150
0.00	39.00	-4.801592	150
0.00	40.00	-5.035196	148
0.00	41.00	-5.283309	150
0.00	42.00	-5.542431	150
0.00	43.00	-5.821033	155
0.00	44.00	-6.115244	194
0.00	45.00	-6.425240	162
0.00	46.00	-6.751153	150
0.00	47.00	-7.092030	185
0.00	48.00	-7.454947	172
0.00	49.00	-7.830948	173
0.00	50.00	-8.226508	179
0.00	51.00	-8.638626	172
0.00	52.00	-9.069971	178
0.00	53.00	-9.519878	191
0.00	54.00	-9.988374	185
0.00	55.00	-10.476139	168
0.00	56.00	-10.982099	138
0.00	57.00	-11.510056	170
0.00	58.00	-12.058821	171
0.00	59.00	-12.628474	178
0.00	60.00	-13.220427	178
0.00	61.00	-13.832880	173
0.00	62.00	-14.473590	177
0.00	63.00	-15.137205	178
0.00	64.00	-15.827974	178
0.00	65.00	-16.545870	188
0.00	66.00	-17.293951	186
0.00	67.00	-18.073139	195
0.00	68.00	-18.887245	184

0.00	69.00	-19.737566	186
0.00	70.00	-20.627750	185
0.00	71.00	-21.561594	191
0.00	72.00	-22.543802	190
0.00	73.00	-23.579075	179
0.00	74.00	-24.673714	215
0.00	75.00	-25.835037	211
0.00	76.00	-27.072275	304
0.00	77.00	-28.397873	258
0.00	78.00	-29.824045	297
0.00	79.00	-31.369724	231
0.00	80.00	-33.056828	297
0.00	81.00	-34.916584	227
0.00	82.00	-36.988480	304
0.00	83.00	-39.333023	258
0.00	84.00	-42.032391	298
0.00	85.00	-45.216888	251
0.00	86.00	-49.106750	297
0.00	87.00	-54.116230	273
0.00	88.00	-61.165161	340
0.00	89.00	-73.211105	810
0.00	90.00	-121.335602	810

Phi	Theta	Alpha=90	BCG Iter
---	-----	-------	--------
0.00	0.00	9.583014	654
0.00	1.00	9.568883	313
0.00	2.00	9.518059	361
0.00	3.00	9.430880	267
0.00	4.00	9.306488	379
0.00	5.00	9.144302	185
0.00	6.00	8.945677	342
0.00	7.00	8.706966	320
0.00	8.00	8.431199	346
0.00	9.00	8.115008	309
0.00	10.00	7.755467	715
0.00	11.00	7.357507	233
0.00	12.00	6.914128	357
0.00	13.00	6.427933	227
0.00	14.00	5.893502	227
0.00	15.00	5.314169	616
0.00	16.00	4.680663	244
0.00	17.00	3.998905	259
0.00	18.00	3.262678	237
0.00	19.00	2.468545	645
0.00	20.00	1.620582	240
0.00	21.00	0.712998	414
0.00	22.00	-0.246950	355

0.00	23.00	-1.256379	585
0.00	24.00	-2.294207	291
0.00	25.00	-3.348589	303
0.00	26.00	-4.366242	563
0.00	27.00	-5.294078	298
0.00	28.00	-6.052021	300
0.00	29.00	-6.583304	333
0.00	30.00	-6.852431	471
0.00	31.00	-6.862307	336
0.00	32.00	-6.692267	299
0.00	33.00	-6.396056	437
0.00	34.00	-6.071772	367
0.00	35.00	-5.737149	333
0.00	36.00	-5.425569	461
0.00	37.00	-5.151746	302
0.00	38.00	-4.928895	436
0.00	39.00	-4.758909	281
0.00	40.00	-4.633798	261
0.00	41.00	-4.560894	461
0.00	42.00	-4.530453	273
0.00	43.00	-4.537940	469
0.00	44.00	-4.588966	444
0.00	45.00	-4.671724	373
0.00	46.00	-4.792987	370
0.00	47.00	-4.940162	474
0.00	48.00	-5.117064	261
0.00	49.00	-5.299952	485
0.00	50.00	-5.510026	381
0.00	51.00	-5.739635	455
0.00	52.00	-5.962952	257
0.00	53.00	-6.203727	481
0.00	54.00	-6.439026	549
0.00	55.00	-6.685131	361
0.00	56.00	-6.921620	539
0.00	57.00	-7.147860	495
0.00	58.00	-7.370139	256
0.00	59.00	-7.572776	505
0.00	60.00	-7.765730	473
0.00	61.00	-7.939365	448
0.00	62.00	-8.096338	511
0.00	63.00	-8.241356	553
0.00	64.00	-8.370316	965
0.00	65.00	-8.479603	455
0.00	66.00	-8.574388	394
0.00	67.00	-8.656987	531
0.00	68.00	-8.726567	477
0.00	69.00	-8.788289	403

```
    0.00      70.00      -8.845181        486
    0.00      71.00      -8.884315        549
    0.00      72.00      -8.905354        387
    0.00      73.00      -8.954330        564
    0.00      74.00      -8.979956        502
    0.00      75.00      -9.005004        541
    0.00      76.00      -9.016927        242
    0.00      77.00      -9.042066        540
    0.00      78.00      -9.054319        244
    0.00      79.00      -9.071721        459
    0.00      80.00      -9.083326        242
    0.00      81.00      -9.100692        461
    0.00      82.00      -9.104582        650
    0.00      83.00      -9.114861        595
    0.00      84.00      -9.124923        241
    0.00      85.00      -9.128168        388
    0.00      86.00      -9.142673        238
    0.00      87.00      -9.138368        151
    0.00      88.00      -9.140660        151
    0.00      89.00      -9.148211        331
    0.00      90.00      -9.147070        140
Cut #  1done
```

---

2 Working principle of AIM-Prism

In this section, we review a finite element - boundary integral formulation for analyzing three dimensional cavity-backed antennas. The finite element discretization is in the form of triangular prisms. Such prisms are the element of choice for modeling planar antennas with fine detail (as small as 50^{th} or 100^{th} of a wavelength) as they require only surface discretization information. In contrast to tetrahedral elements [6], this eliminates the need to generate volume meshes which could be tedious and also removes the possibility of ill-conditioned systems due to degraded mesh quality. In general, for modeling planar configurations the prism element also requires lesser number of unknowns than tetrahedral elements. However, very small details and consequently dense meshes can still lead to boundary integrals with extremely large computational requirement. In the previous section it was shown that AIM reduces the computational requirement considerably. In this section, we present the key elements of a three dimensional finite element - boundary integral formulation with emphasis on the boundary integral computation. For details on the prism element the reader is referred to [7].

Consider a cavity-backed antenna recessed in a ground plane as depicted in Figure 14. To solve for the E-field inside and on the aperture of the cavity, it is necessary to extremize a functional, which for radiation and scattering problems may be generalized as

$$F(\mathbf{E}) \;=\; \frac{1}{2}\iiint_V \{(\nabla\times\mathbf{E})\cdot\bar{\bar{\mu}}_r^{-1}\cdot(\nabla\times\mathbf{E}) - k_0^2\mathbf{E}\cdot\bar{\bar{\epsilon}}_r\cdot\mathbf{E}\}dV$$

$$+ \iiint_{V_s} \mathbf{E} \cdot \left(jk_0 Z_0 \mathbf{J}^i + \nabla \times \bar{\bar{\mu}}_r^{-1} \cdot \mathbf{M}^i \right) dV$$
$$+ jk_0 Z_0 \iint_{S_0+S_f} \mathbf{E} \cdot (\mathbf{H} \times \hat{n}) dS \tag{33}$$

where $\bar{\bar{\epsilon}}_r$ and $\bar{\bar{\mu}}_r$ denote the relative tensor permittivity and permeability of the cavity filling, S_0 represents the non-metallic portions of the aperture and S_f denotes the junction opening to the feeding structures. The volume V_s refers to the volume occupied by the impressed sources $\mathbf{J}_i$ and $\mathbf{M}_i$. Also, $\mathbf{H}$ denotes the magnetic field on S_0 or S_f and $\hat{n}$ is the outer normal to these surfaces.

For a unique solution of $\mathbf{E}$ we require knowledge of $\mathbf{H}$ over S_0 and S_f . In the case of S_f, $\mathbf{H}$ is determined by the feed excitation while that over the non-metallic portions of the aperture is determined by the boundary integral equation

$$\mathbf{H} = \mathbf{H}^{go} + 2jk_0 Y_0 \iint_{S_0} \bar{\mathbf{G}}(\mathbf{r}, \mathbf{r}') \cdot (\hat{z} \times \mathbf{E}(\mathbf{r}')) \; dS' \tag{34}$$

where $\bar{\mathbf{G}}$ is the electric dyadic Green's function of the first kind such that $\hat{n} \times \bar{\mathbf{G}} = 0$ is satisfied on the metallic platform. For the cavity recessed in a ground plane, $\bar{\mathbf{G}}$ becomes the half space dyadic Green's function

$$\bar{\mathbf{G}} = \left(\bar{\mathbf{I}} + \frac{1}{k_0^2} \nabla\nabla \right) \frac{e^{-jk_0 R}}{4\pi R} \tag{35}$$

with R = $|\mathbf{r} - \mathbf{r}'|$ and $\bar{\mathbf{I}}$ is the unit dyad. For this problem, $\mathbf{H}^{go}$ is equal to the sum of the incident and reflected fields for scattering computations and zero for antenna analysis. To discretize (33) the volume region is subdivided using prismatic elements. The field in each prism is approximated using a linear edge-based expansion as

$$\mathbf{E}^e = \sum_{j=1}^{9} E_j^e \mathbf{V}_j^e = [\mathbf{V}]_e^T \{E^e\} \tag{36}$$

where $[\mathbf{V}]_e = [\{V_x\}, \{V_y\}, \{V_z\}]$ and $\{E^e\} = \{E_1^e, E_2^e, \ldots, E_9^e\}^T$. On the aperture, since the top and bottom faces of the prism are triangles, we have a corresponding representation for the aperture fields as

$$\mathbf{E}^s(\mathbf{r}) = \sum_{i=1}^{3} E_i^s \mathbf{S}_i^s(\mathbf{r}) = [S]_s^T \{E^s\} \tag{37}$$

where $[S]_s = [S_x, S_y]$.

To generate a linear system for the solution of E_j^e, (36) and (37) are substituted into (33). Subsequent minimization of the functional yields

$$\left\{ \frac{\partial F_V}{\partial E^e} \right\} = \sum_{e=1}^{N_v} [A^e]\{E^e\} + \sum_{s=1}^{N_s} [B^s]\{E^s\} + \sum_{e=1}^{N_v} \{K^e\} + \sum_{s=1}^{N_s} \{L^s\} = 0 \tag{38}$$

where N_v and N_s indicate the number of volume and surface elements, respectively. The matrix elements are given by

$$A_{ij}^e = \iiint_{V_e} \{(\nabla \times \mathbf{V}_i) \cdot \bar{\bar{\mu}}_r^{-1} \cdot (\nabla \times \mathbf{V}_j) - k_0^2 \mathbf{V}_i \cdot \bar{\bar{\epsilon}}_r \cdot \mathbf{V}_j\} dV \tag{39}$$

$$K_e^i = \iiint_{V_e} \mathbf{V}_i \cdot \left[jk_0 Z_0 \mathbf{J}^i + \nabla \times \bar{\bar{\mu}}_r^{-1} \cdot \nabla \times \mathbf{M}^i \right] dV \tag{40}$$

$$\begin{aligned} B_{ij}^s &= -\iint_{S_s} \iint_{S_s'} 2k_0^2 \mathbf{S}_i^s(\mathbf{r}) \cdot \mathbf{S}_j^s(\mathbf{r}') G_0(\mathbf{r}, \mathbf{r}') dS dS' \\ &+ 2 \iint_{S_s} \iint_{S_s'} [\nabla \times \mathbf{S}_i^s(\mathbf{r})]_z [\nabla' \times \mathbf{S}_j^s(\mathbf{r}')]_z G_0(\mathbf{r}, \mathbf{r}') dS dS' \end{aligned} \tag{41}$$

$$L_i^s = 2jk_0 Z_0 \iint_{S_s} S_i^s \cdot (\mathbf{H}^i \times \hat{z}) dS \tag{42}$$

The boundary integral equation in (41) is discretized using basis functions defined on the top face of the prism as

$$\mathbf{S}_i = \frac{l_i}{2A^e} \hat{z} \times (\mathbf{r} - \mathbf{r}_i) \tag{43}$$

similar to the function defined in (9). Substitution of (43) into (41) gives the discretized boundary integral which is treated using the procedure outlined in Section 1.

Several cavity-backed antennas contain small features and details which may necessitate high discretization. This could take the form of very narrow slots which may be a fiftieth or hundredth of a wavelength in width. Discretization of such geometries could lead to very large numerical systems even if the size of the antenna is not electrically very large. To efficiently treat such systems, the properties of an algorithm based on an iterative solver, should include the following

- It is of paramount importance that the "threshold" distance (distance beyond which interactions are treated as of the far zone variety) is as small as possible.
- It should be capable of characterizing small perturbations in an otherwise smooth surface.
- It should be capable of modeling near fields accurately.
- If the algorithm incorporates a process by which very small discretization details can be "mapped" onto a different domain which is less dense than the original, computation of the matrix vector product in this domain would simulate the effect of a reduced number of unknowns.

Figures 8 and 9 depict two planar configurations analyed by the AIM from which it can be gleaned that all the above criteria are met. Unlike FMM, which carries out the matrix vector product on the original moment method discretization, the ability of AIM to map the small details onto a sparse grid and still retain accuracy makes it the method of choice to analyse such antennas. For efficient modeling of the cavity we employ FEM with its low $O(N)$ storage and execution time. Triangular prisms are used for discretization of the cavity volume for the reasons described in [7].

2.1 Implementation

The FE-BI formulation for three dimensional cavity-backed antennas using prismatic elements is described in the previous section. Substitution of (43) in (41) gives a discretized boundary integral of the form in (15). The near and far zone terms are treated as outlined in 1.1. The FEM matrix and the near zone interactions of AIM are stored in a sparse storage format, thus affecting significant savings in memory.

2.2 Results

Figure 15 shows the radiation pattern for an annular slot computed in the elevation plane, $\phi = 5^0$. The reference FE-BI solution [7] is contrasted with computations of BI using AIM (indicated as FE-AIM). It is seen that for this example, the threshold distance in AIM can be reduced to 0.25λ without significant loss of accuracy. This enables the reduction of matrix entries stored in the near field portion by a factor of three resulting in a corresponding savings in memory as indicated in the tabulation of the near-zone non-zero entries. Figure 16 shows the radiation pattern for the same antenna in the $\phi = 90^0$ elevation plane. The normal direction in this plane, reveals the characteristic separation between co-polarization and cross-polarization levels for the annular slot at observation angles close to normal in the elevation plane. From this figure, it is gleaned that the threshold distance in AIM can be reduced down to even 0.15λ if an average error of a dB could be tolerated. From the computation of near-zone matrix entries, such a threshold would result in a factor of five saving in memory. Figure 17 shows a scattering cross-section for the same slot but at a frequency of 0.73 GHz (at which the antenna is electrically even smaller) instead of the previous 1 GHz. It should be noted that for a threshold of 0.4λ (larger than the diameter of the BI contour) the near-zone and far-zone entries for AIM cancel each other in accordance with (31), thus yielding a very small error (0.00086 dB) in comparison to the FE-BI solution. A quantity of vital importance in antenna computations is input impedance. Figure 18 depicts the input impedance of a very narrow probe-fed annular slot, computed using FE-BI and FE-AIM. The probe is placed at $y = 0$. It is seen that evaluation of the boundary integral with AIM enables the reduction of the near-zone non-zeros by more than half. Computation of input impedance demands very high accuracy and the threshold distance was held constant at 10.5 cm (corresponding to 0.35λ at 1 GHz and 0.49λ at 1.4 GHz - the corresponding diameter of the entire BI contour varying from 0.513λ to 0.718λ). While, Figures 15-18 demonstrate the ability of AIM to translate very fine details such as a narrow slot onto a coarser equivalent grid, Figure 19 and 20 indicate the importance of a low threshold distance in modeling cavity-backed antenna arrays. Figure 19 and 20 indicate that for an average error of less than a dB in scattering and radiation patterns it is possible to reduce the number of non-zeros in the near-zone part of the impedance matrix by a factor of six, resulting in substantial saving in memory. This is a consequence of employing a threshold distance of 10 cm, which is about a fifth of the cavity diameter. It is necessary to note that employing such a threshold distance results in a majority of the interactions between different slots being treated with the AIM procedure. This is of paramount importance in modeling antenna arrays and spiral antennas. While Figures 15-19 compare spatial domain FE-BI and FE-AIM solutions, Figure 21 compares the spatial domain FE-AIM solution with a spectral-domain FE-BI solution presented in [8] for the scattering by a cavity-backed patch antenna.

2.3 Summary

AIM, with its low threshold distance, and ability to translate to an equivalent grid is capable of saving a significant amount of memory and solution time for bodies which are finely discretized even though they may not be electrically large. Its accuracy is preserved even while performing radiation computations thus making it the method of choice for analyzing antennas with intricate details.

2.4 AIM-Prism execution

Computation of radiation with AIM-Prism is a three step process, however for the geometry in Figure 18 step one and two have already been executed and are listed merely to aid future development

1. Mesh the antenna geometry of choice. AIM-Prism requires just a surface mesh since it employs prismatic elements. The surface mesh needs to have the following details

   - Triangles in the slots need to be grouped.
   - Nodes in the slots nees to be grouped.
   - Boundary nodes belong to both metal and aperture groups.
   - Corner nodes need to be grouped.
   - Nodes between which probes are connected need to be grouped

   A universal file (level 6 IDEAS) meeting these specifications is `ring_slot.unv` which contains the geometry depicted in Figure 18. It is processed with the pre-processor `shell_level6.f` to extract the above information. A dimension file `DIM.INC` along with other subsidiary files is written as a result of the pre-processing operation. `DIM.INC` needs to be augmented with information from the AIM pre-processor executed in step 2 before it is complete. A transcript of the session with the IDEAS level 6 pre-processor is indicated below.

```
[ 412 ] temp -: shell_level6
 NAME OF UNIVERSAL FILE ?
ring_slot.unv

 ENCOUNTERED HEADER
 THERE ARE 270 NODES.
 THERE ARE 512 ELEMENTS.
 THERE ARE 96 NODES ON THE SLOTS
 THERE ARE 96 ELEMENTS ON THE SLOTS
 THERE ARE 26 NODES ON THE EDGE OF TOP
 THERE ARE  2 PROBES IN THE SYSTEM
 BE PATIENT !!!  COUNTING EDGES...
 EDGE COUNT =  781
 PROCESSING SLOT FOR ON-SURFACE EDGES...
   96 SLOT SURFACE-TRIANGLES.
 THERE ARE  192  SLOT EDGES AND  96  NONPEC'S
   685 EDGES ON THE PEC SURFACE
```

2. The AIM pre-processor determines dimension parameters related to the boundary integral. This program `PreProcAnt.f` produces the following output

```
[ 343 ] AIMPrism.dir -: !!
PreProcAnt
 maxx= 8.075
```

```
 minx= -8.075
 maxy= 8.06903
 miny= -8.06903

 Input frequency at which the structure will be
 analyzed (GHz)
1.35

 Enter AIM grid step in WAVELENGTHS (0.05 suggested)
 Note: The main AIM code has been hard-wired for
 0.05 lambda but can be easily changed to 0.1 lambda
 by changing the variable step
.05

 nx in main progam to be=  19
 ny in main progam to be=  19
 FFT order along x (iFFTx in main pgm) 64
 FFT order along y (iFFTy in main pgm) 64
 maxnod= 96
 maxedg= 192
 maxtri= 96
 nmax= 50
 nintedg= 96
 ntris= 96
 Order of system =  96
 No. of triangular elements =  96


 Enter near field threshold in CENTIMETER
 Note: This is related to the Maximum
 number of non-zeros in the near-field matrix
 Recommend this to be 0.2-0.7 times the
 wavelength in centimeter. This is a
 empirical quantity and needs to be
 determined by trial & error
10.5
 Set number of nonzeros in Near Z = 2245
```

As a result of this the dimension file `DIM.INC` is augmented by the following few lines

```
Parameter (nonzero=2245)
Parameter (nx=19)
Parameter (ny=19)
Parameter (iFFTx=64)
Parameter (iFFTy=64)
Parameter (ordermax=10)
```

3. AIM-Prism is then executed and an example which produces the input impedance at

1.35 GHz for the annular slot ring is depicted below

```
[ 347 ] AIMPrism.dir -: NewPrism
 ****** USER-ORIENTED DATA INTERFACE ******
 ******************************************

 INPUT CAVITY HEIGHT AND NUM. OF SGMTS. ALONG Z
3 2
 INPUT SEGMENT SIZE ALONG Z AXIS FROM TOP TO BTM.
 ENTER THE HEIGHT FOR SEGMENT  1(1 REAL)
1.5
 ENTER THE HEIGHT FOR SEGMENT  2(1 REAL)
1.5

 INPUT NUMBER OF DIELECTRIC LAYERS (1 INTGR)
1

 ASSUME THE LAYERS ARE COUNTED FROM THE BOTTOM, THUS
 EP,EU (2 CMPLX) & NUM. OF SEMS. (1 INTGR) FOR LAYER  1
(1.35,0.) (1.,0.) 2
 ENTER PATTERN (1-BISTATIC,2-BACKSCATTER,3-RADIATION):
3
 ENTER FEED STYLE: (1-VERTICAL,2-HORIZONTAL)
2
 ENTER FREQ. (IN GHz):
1.35
 ENTER: 1-RADIATION PATTERN,2-INPUT IMPEDANCE,3-GAIN
2
 ENTER TOLERANCE (eg. 0.0001) FOR BICG ITERATIONS:
.001
 ABOVE DATA O.K. (1-YES, 2-NO)?
1
 TOTAL PEC EDGES:  1544
 TOTAL NUMBER OF NON-PEC EDGES:  1339<  2400
 TOTAL NUMBER OF EDGES:  2883< 4000

 DONE WITH FEM MATRIX FILLING!

 Equivalence coefficients computed now
 50 elements done
 Toeplitz G calculation


 Enter near field threshold in CENTIMETER
 Note: This is related to the Maximum
 number of non-zeros in the matrix
 Recommend this to be 0.2-0.7 times the
```

```
 wavelength in centimeter. This is a
 empirical quantity and needs to be
 determined by trial & error
10.5
 50 elements done
 DONE WITH BI MATRIX FILLING!

 NS 2 3
 FINISH COMBINING!  START BICG ITERATION...
 Iteration number  1 Residual  .9794996
 Iteration number  2 Residual  1.17442
 Iteration number  3 Residual  1.21015
 Iteration number  4 Residual  .8353357



 Iteration number  1146 Residual  4.96248E-03
 Iteration number  1147 Residual  7.29750E-03
 Iteration number  1148 Residual  2.34599E-03
 Iteration number  1149 Residual  2.00533E-03
 Iteration number  1150 Residual  1.48691E-03
 Iteration number  1151 Residual  2.24077E-03
 Iteration number  1152 Residual  1.99295E-03
 1152 TIMES ITERATIONS!
 1.35 59.84542 -67.166
```

2.4.1 Cavity-backed slot array analysis

For the slot array of Figure 20, the procedure for the single slot discussed above differs in a few respects. The universal file is an IDEAS Master Series 2.1 which is converted with a new pre-processor `shellMSC.f`. Also, for the radiation pattern each of the four slots is fed and the file containing the probe feeds ESOURCE is correspondingly augmented. The transcript of the slot array run is indicated below

```
****** USER-ORIENTED DATA INTERFACE ******
 ******************************************

 INPUT CAVITY HEIGHT AND NUM. OF SGMTS. ALONG Z
1.5 1
 INPUT SEGMENT SIZE ALONG Z AXIS FROM TOP TO BTM.
 ENTER THE HEIGHT FOR SEGMENT  1(1 REAL)
1.5

 INPUT NUMBER OF DIELECTRIC LAYERS (1 INTGR)
1

 ASSUME THE LAYERS ARE COUNTED FROM THE BOTTOM, THUS
 EP,EU (2 CMPLX) & NUM. (2,0) (1,0) 1
```

```
 OF SEMS. (1 INTGR) FOR LAYER  1
 ENTER PATTERN (1-BISTATIC,2-BACKSCATTER,3-RADIATION):
1
 ENTER FEED STYLE: (1-VERTICAL,2-HORIZONTAL)
2
 ENTER FREQ. (IN GHz):
1
 ENTER E-FIELD POLARIZATION ANGLE ALPHA (IN DEGREES):
0
 ENTER ANGLES OF INCIDENCE...
 PHI (IN DEGREES):
0
 THETA (IN DEGREES):
0
 ENTER CUT SPECIFICATIONS...
 FIX (1-PHI, 2-THETA):
1
 ENTER FIXED OBSERVATION ANGLE PHI (IN DEGREES):
90
 ENTER START OBSERVATION ANGLE THETA (IN DEGREES):
0
 ENTER STOP OBSERVATION ANGLE THETA (IN DEGREES):
90
 ENTER NUMBER OF OBSERVATION POINTS:
90
 ENTER TOLERANCE (eg. 0.0001) FOR BICG ITERATIONS:
0.001
 ABOVE DATA O.K. (1-YES, 2-NO)?
1
 TOTAL PEC EDGES:  4546
 TOTAL NUMBER OF NON-PEC EDGES:  983<  2500
 TOTAL NUMBER OF EDGES:  5529< 6000

 Equivalence coefficients computed now
 50 elements done
 100 elements done
 150 elements done
 200 elements done
 Toeplitz G calculation


 Enter near field threshold in CENTIMETER
 Note: This is related to the Maximum
 number of non-zeros in the matrix
 Recommend this to be 0.2-0.7 times the
 wavelength in centimeter. This is a
 empirical quantity and needs to be
```

```
 determined by trial & error
10
 50 elements done
 100 elements done
 150 elements done
 200 elements done
 FINISH COMBINING!  START BICG ITERATION...
 Iteration number  1 Residual  1.22629
 Iteration number  2 Residual  2.06872
 Iteration number  3 Residual  2.49931
 Iteration number  4 Residual  4.67545
 Iteration number  5 Residual  10.21917


 Iteration number  210 Residual  1.20682E-03
 Iteration number  211 Residual  1.37842E-03
 Iteration number  212 Residual  1.62599E-03
 Iteration number  213 Residual  1.42027E-03
 Iteration number  214 Residual  1.17562E-03
 Iteration number  215 Residual  1.14276E-03
 Iteration number  216 Residual  1.03158E-03
 216 TIMES ITERATIONS!
 .0 1.0 3.33673 3.33345 -27.88
 1.01124 1.0 3.32997 3.32668 -27.8791
 2.02247 1.0 3.30988 3.30659 -27.9024
 3.03371 1.0 3.27648 3.27321 -27.95
 4.04494 1.0 3.22976 3.2265 -28.0221
 5.05618 1.0 3.16974 3.16652 -28.1189
 6.06742 1.0 3.09644 3.09325 -28.2408
 7.07865 1.0 3.00988 3.00673 -28.3883
 8.08989 1.0 2.91008 2.90698 -28.5618
 9.10112 1.0 2.79706 2.79403 -28.7618
 10.11236 1.0 2.67086 2.6679 -28.9893
 11.12359 1.0 2.53152 2.52864 -29.2448
 12.13483 1.0 2.37908 2.37628 -29.5295
 13.14606 1.0 2.21356 2.21086 -29.8444
 14.1573 1.0 2.03503 2.03243 -30.1909
 15.16853 1.0 1.84355 1.84106 -30.5706
 16.17977 1.0 1.63916 1.63679 -30.9851
 17.191 1.0 1.42192 1.41967 -31.4368
 18.20224 1.0 1.19191 1.1898 -31.9281
 19.21347 1.0 .9492078 .9472271 -32.4619
 20.22471 1.0 .6938675 .6920296 -33.042
 21.23595 1.0 .4259951 .4243047 -33.6726
 22.24718 1.0 .1456651 .1441254 -34.359
 23.25842 1.0 -.147019 -.148405 -35.1076
 24.26965 1.0 -.451955 -.453187 -35.9264
```

```
25.28089 1.0 -.769034 -.770111 -36.8255
26.29212 1.0 -1.09814 -1.09906 -37.8173
27.30336 1.0 -1.43913 -1.43991 -38.9179
28.31459 1.0 -1.79191 -1.79254 -40.1475
29.32583 1.0 -2.15631 -2.15681 -41.5314
30.33706 1.0 -2.53218 -2.53256 -43.0985
31.3483 1.0 -2.91937 -2.91965 -44.8732
32.35954 1.0 -3.31771 -3.3179 -46.8398
33.37077 1.0 -3.72701 -3.72714 -48.8261
34.38201 1.0 -4.14708 -4.14719 -50.2623
35.39325 1.0 -4.57773 -4.57784 -50.333
36.40449 1.0 -5.01873 -5.0189 -49.1148
37.41572 1.0 -5.46987 -5.47015 -47.4428
38.42696 1.0 -5.9309 -5.93134 -45.8266
39.4382 1.0 -6.40157 -6.40226 -44.4074
40.44944 1.0 -6.88162 -6.88264 -43.1915
41.46067 1.0 -7.37077 -7.37221 -42.1526
42.47191 1.0 -7.86873 -7.87072 -41.2613
43.48315 1.0 -8.37518 -8.37785 -40.4927
44.49438 1.0 -8.88983 -8.89334 -39.8265
45.50561 1.0 -9.41234 -9.41686 -39.2468
46.51685 1.0 -9.94237 -9.9481 -38.7407
47.52809 1.0 -10.4796 -10.4867 -38.2981
48.53932 1.0 -11.0236 -11.0325 -37.9106
49.55056 1.0 -11.574 -11.5849 -37.5716
50.5618 1.0 -12.1305 -12.1438 -37.2752
51.57304 1.0 -12.6927 -12.7088 -37.0168
52.58427 1.0 -13.2602 -13.2795 -36.7923
53.59551 1.0 -13.8327 -13.8557 -36.5982
54.60675 1.0 -14.4097 -14.437 -36.4314
55.61799 1.0 -14.9909 -15.0233 -36.2893
56.62923 1.0 -15.5761 -15.6141 -36.1695
57.64046 1.0 -16.1648 -16.2094 -36.07
58.65169 1.0 -16.7569 -16.809 -35.9887
59.66293 1.0 -17.352 -17.4127 -35.9241
60.67417 1.0 -17.9499 -18.0206 -35.8744
61.6854 1.0 -18.5507 -18.6325 -35.8384
62.69664 1.0 -19.1541 -19.2488 -35.8145
63.70788 1.0 -19.7601 -19.8696 -35.8017
64.71912 1.0 -20.3689 -20.4952 -35.7986
65.73035 1.0 -20.9807 -21.1262 -35.804
66.74159 1.0 -21.5957 -21.7632 -35.8174
67.75283 1.0 -22.2143 -22.4071 -35.8374
68.76406 1.0 -22.8371 -23.059 -35.8631
69.77529 1.0 -23.4647 -23.7203 -35.8937
70.78653 1.0 -24.0979 -24.3926 -35.9283
71.79777 1.0 -24.7377 -25.078 -35.9661
```

```
 72.80901 1.0 -25.3852 -25.779 -36.0064
 73.82025 1.0 -26.0418 -26.4986 -36.0485
 74.83148 1.0 -26.7087 -27.2406 -36.0916
 75.84272 1.0 -27.3875 -28.0095 -36.1351
 76.85396 1.0 -28.0799 -28.811 -36.1784
 77.86519 1.0 -28.7873 -29.6521 -36.2209
 78.87643 1.0 -29.5111 -30.5419 -36.2621
 79.88767 1.0 -30.252 -31.4919 -36.3015
 80.89891 1.0 -31.0102 -32.5172 -36.3385
 81.91014 1.0 -31.7837 -33.6386 -36.3728
 82.92137 1.0 -32.5682 -34.8851 -36.404
 83.93262 1.0 -33.3545 -36.2989 -36.4318
 84.94385 1.0 -34.1269 -37.9457 -36.4558
 85.95509 1.0 -34.8596 -39.9356 -36.4758
 86.96633 1.0 -35.5149 -42.4744 -36.4915
 87.97756 1.0 -36.0433 -46.0249 -36.5029
 88.9888 1.0 -36.3905 -52.0628 -36.5098
 90.00004 1.0 -36.5121 -80.0 -36.5121
141.03u 0.22s 2:33.22 92.1%
```

References

[1] T.B.A. Senior and J.L. Volakis, *Approximate boundary conditions in electromagnetics.* IEE press: London, 1995.

[2] S. Rao, D. Wilton, and A. Glisson, "Electromagnetic scattering by surfaces of arbitrary shape," *IEEE Transactions on Antennas and Propagation*, vol. 30, no. 3, pp. 409–418, 1982.

[3] D.R. Wilton, S.M. Rao, A.W. Glisson, D.H. Schaubert, O.M. Al-Bundak, and C.M. Butler, "Potential integrals for uniform and linear source distributions on polygonal and polyhedral domains," *IEEE Transactions on Antennas and Propagation*, vol. 32, pp. 276–281, March 1984.

[4] E. Bleszynski, M. Bleszynski, and T. Jaroszewicz, "AIM: Adaptive integral method for solving large-scale electromagnetic scattering and radiation problems," *Radio Science*, vol. 31, no. 5, pp. 1225–1251, 1996.

[5] S. S. Bindiganavale and J. L. Volakis, "Guidelines for using the fast multipole method to calculate the RCS of large objects," *Microwave and Optical Technology Letters*, vol. 11, no. 4, pp. 190–194, 1996.

[6] J. Gong, J.L. Volakis, and A.C. Woo, "A hybrid finite element-boundary integral method for the analysis of cavity-backed antennas of arbitrary shape," *IEEE Transactions on Antennas and Propagation*, vol. 42, no. 9, pp. 1233–1242, 1994.

[7] J. Gong, J.L. Volakis, and H.T.G. Wang, "Efficient finite element simulation of slot antennas using prismatic elements," *Radio Science*, vol. 31, no. 6, pp. 1837–1844, 1996.

[8] A.C. Polycarpou, M.R. Lyons, J. Aberle, and C.A. Balanis, "Analysis of arbitrary shaped cavity-backed patch antennas using a hybritization of the finite element and spectral domain methods," in *1996 IEEE Int. Symp. on Antennas and Propagation Digest*, July 1996.

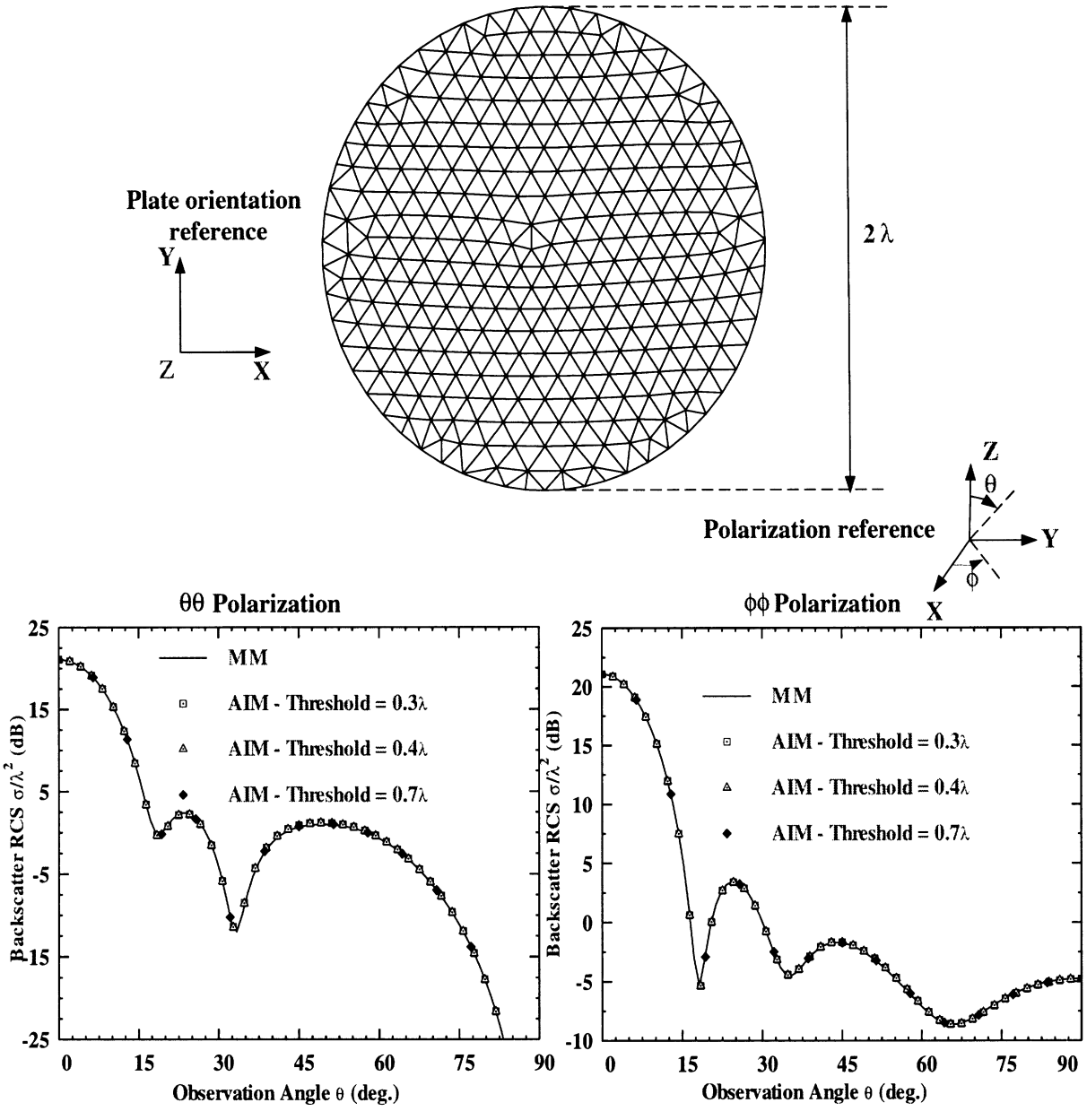

Figure 4: Monostatic RCS for a circular plate of diameter 2λ; Comparison of the standard MM & AIM

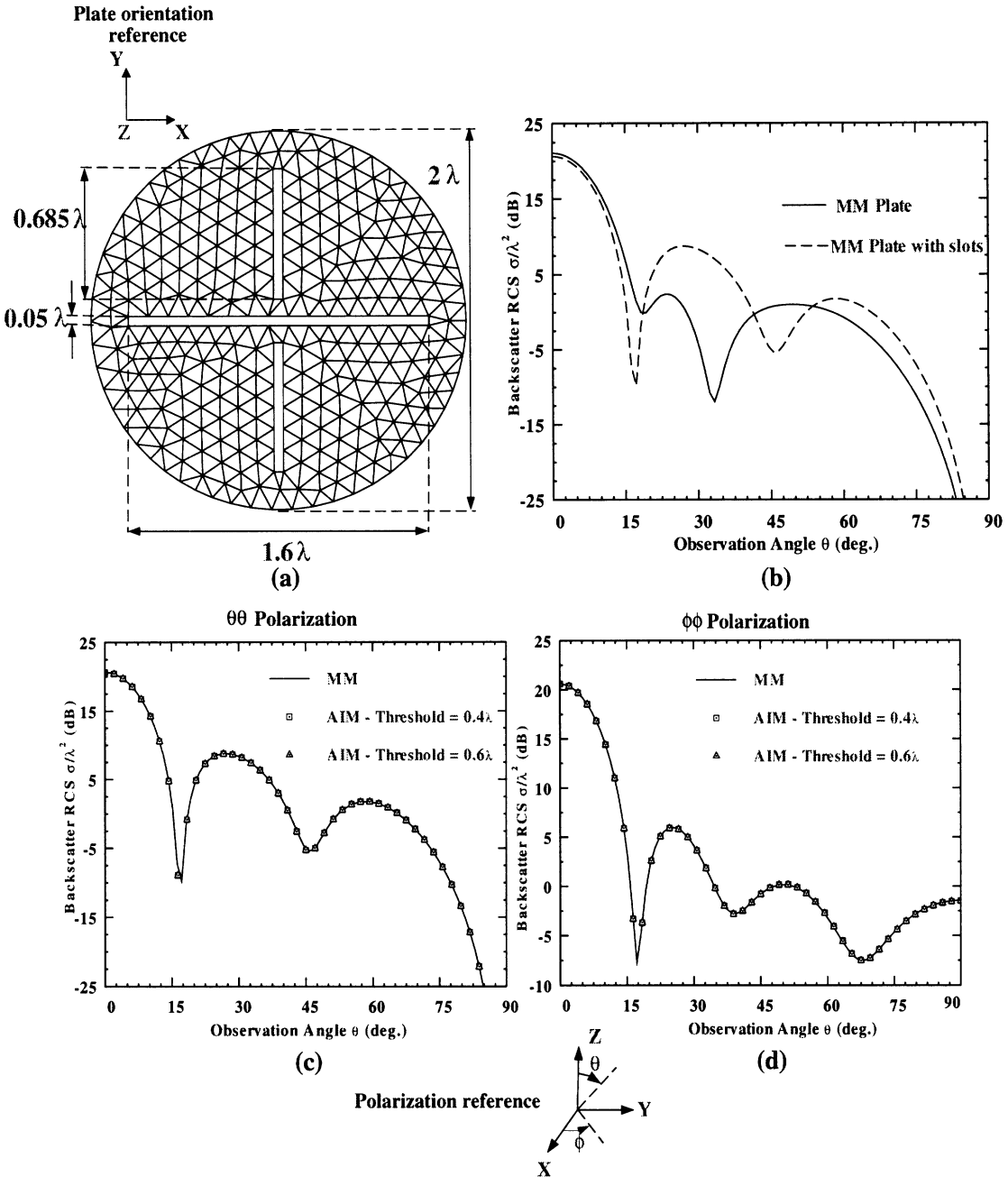

Figure 5: Monostatic RCS for a circular plate of diameter 2λ with three slots computed with standard MM & AIM (a) Geometry (b) Effect of the slots on the RCS (c) $\theta\theta$ polarization backscatter RCS for the plate with slots (d) $\phi\phi$ polarization backscatter RCS for the plate with slots

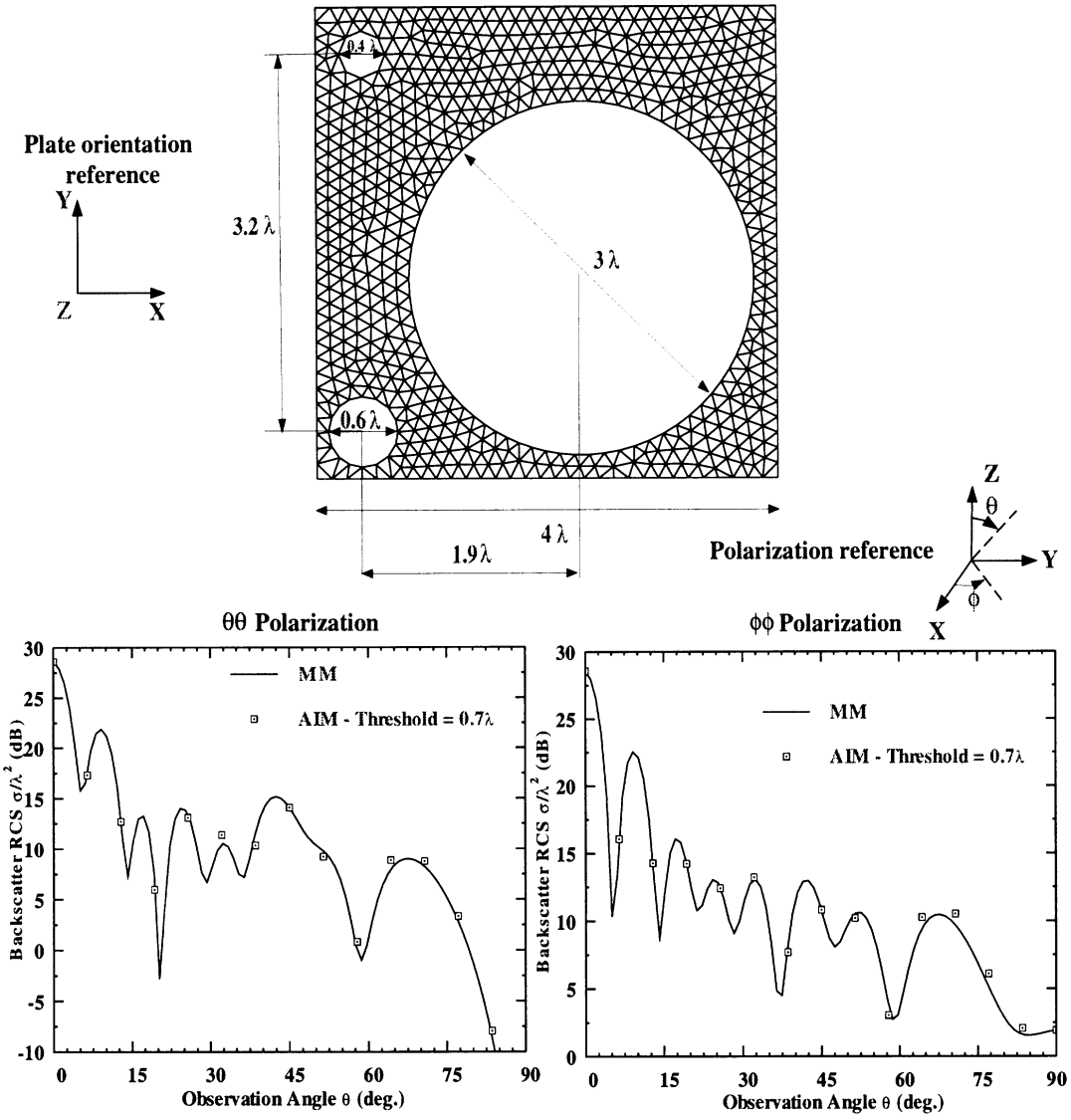

Figure 6: Monostatic RCS for a square plate of side 4λ with three holes computed with standard MM & AIM

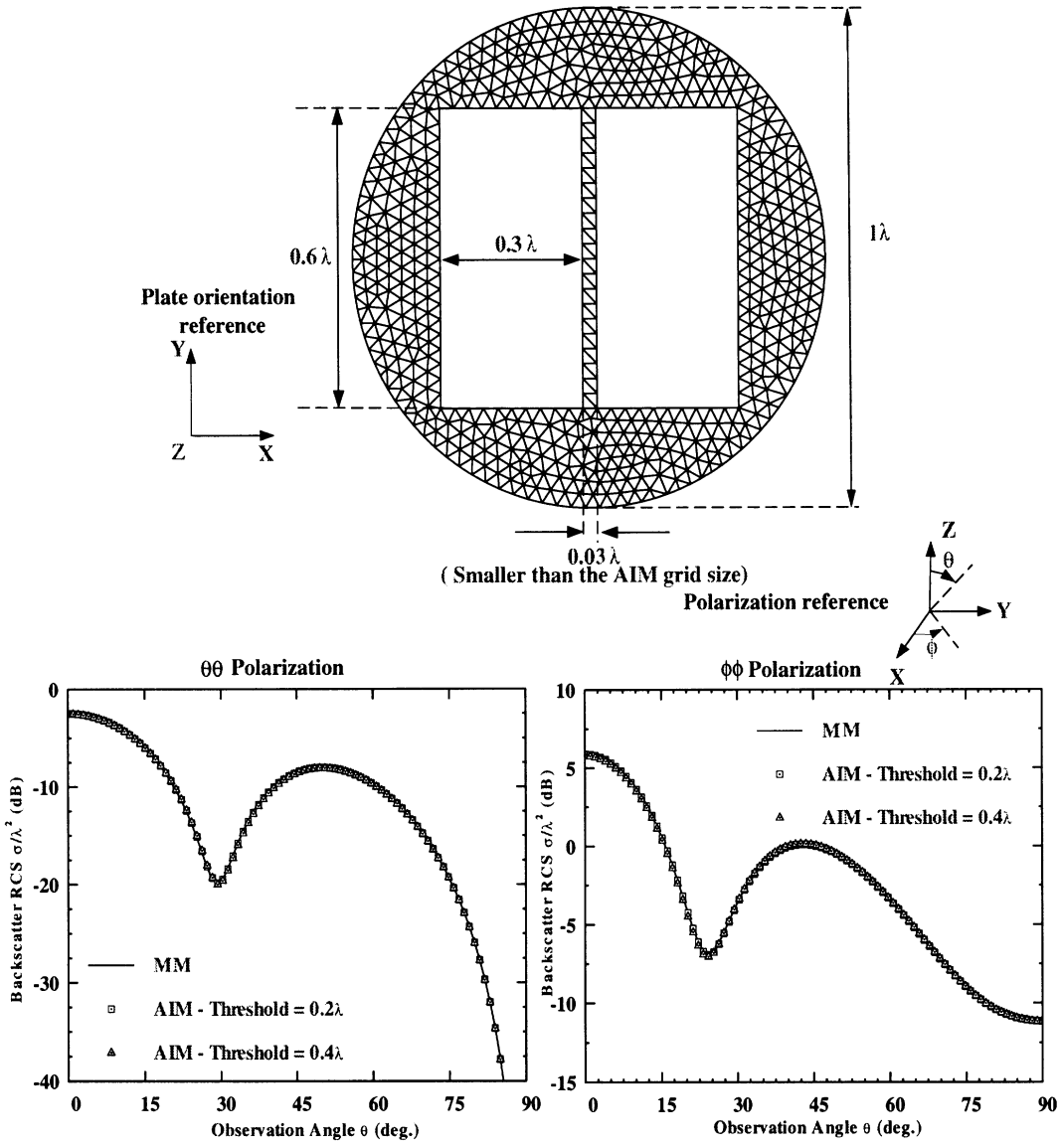

Figure 7: Monostatic RCS for a circular plate of diameter 1λ sampled at 0.03 λ (smaller than the AIM grid spacing) due to the narrow center ridge

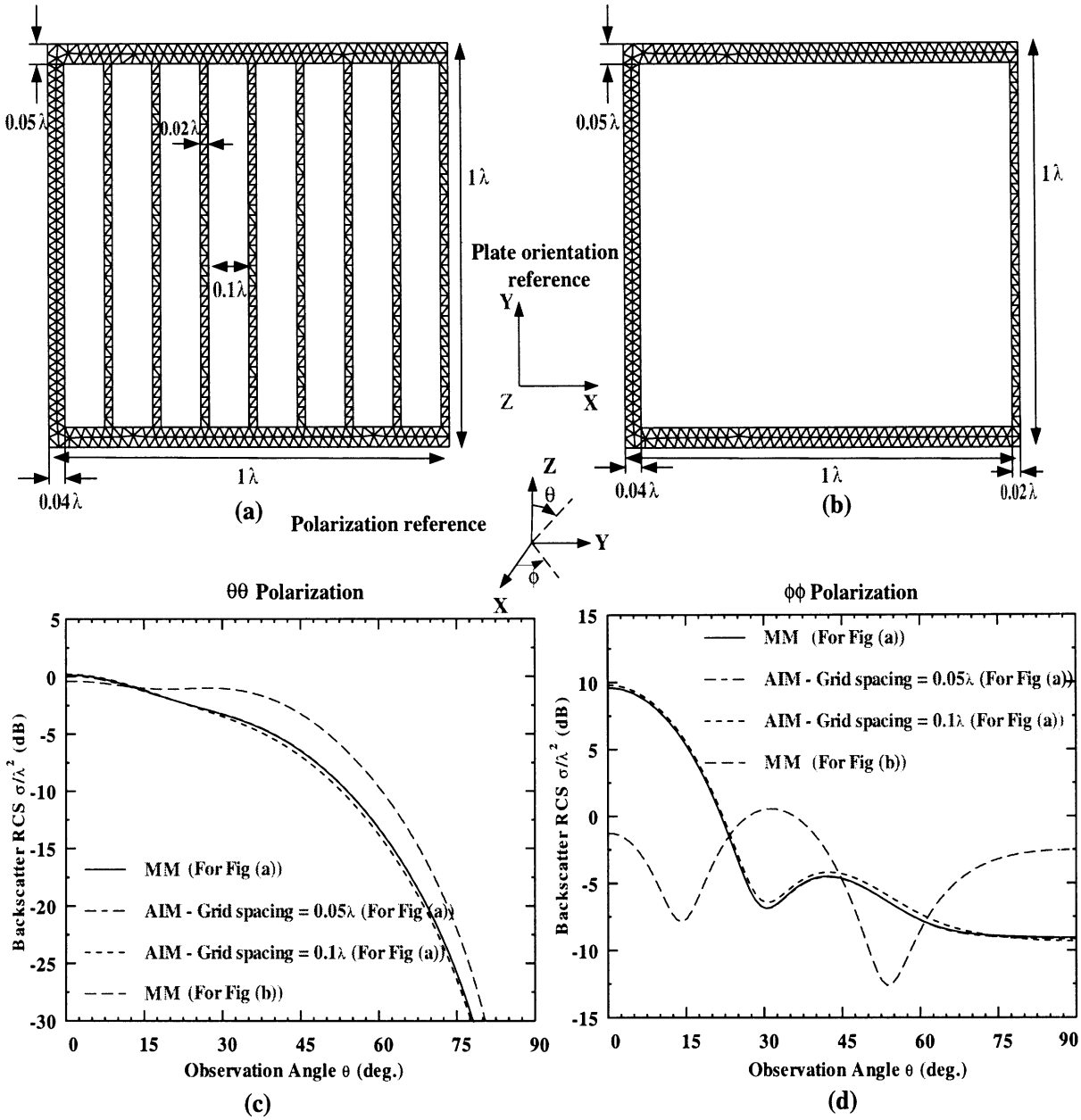

Figure 8: (a) Geometry and mesh of the grated plate (b) Geometry and mesh of the "Groove" plate without gratings (c) $\theta\theta$ polarization backscatter RCS computed by AIM and MM (d) $\phi\phi$ polarization backscatter RCS computed by AIM and MM

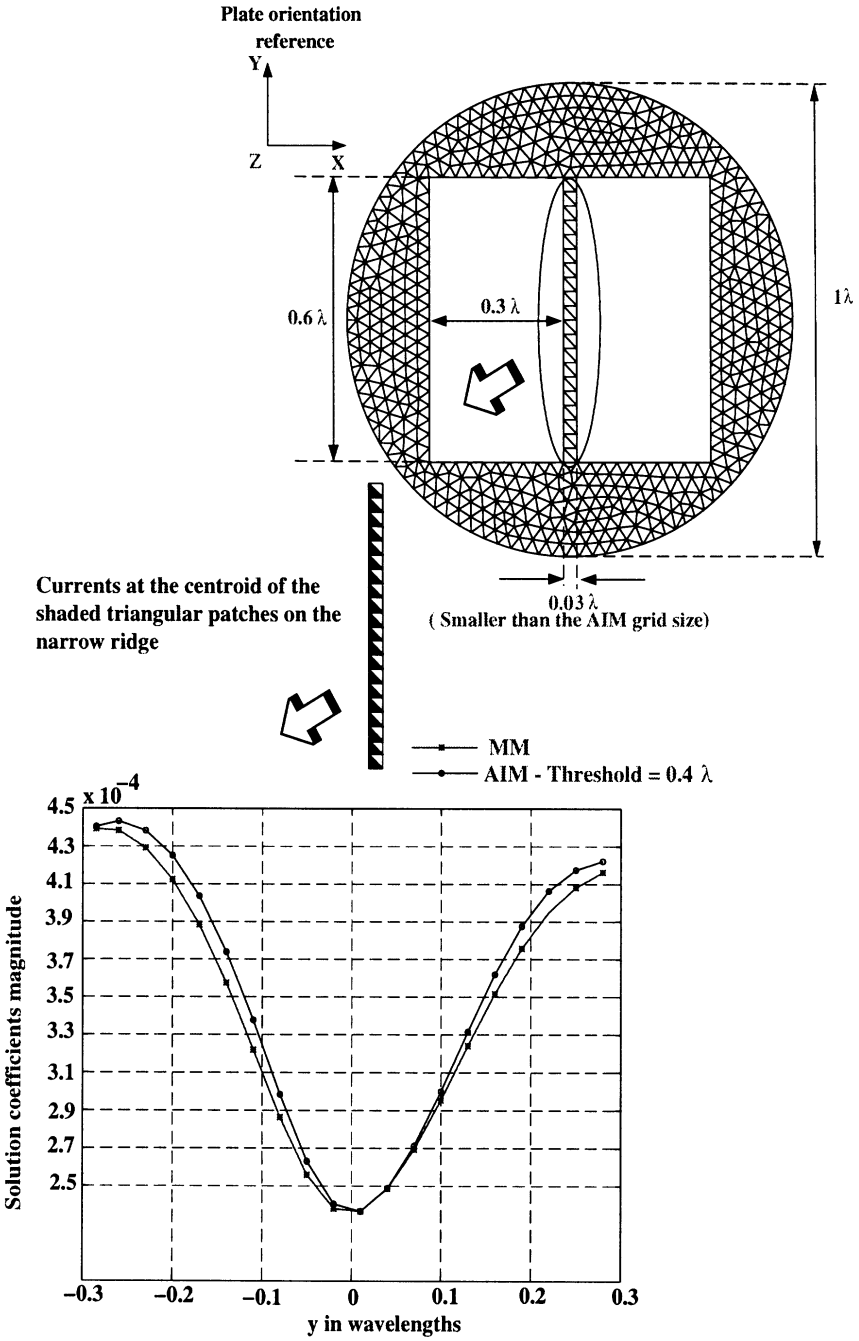

Figure 9: Electric currents (Solution coefficients) on the narrow ridge for the geometry of Figure 7

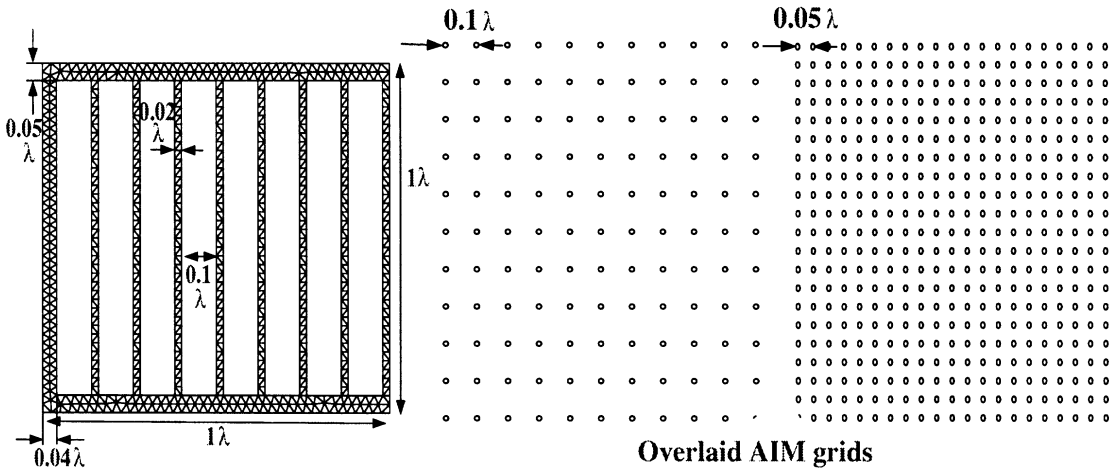

Figure 10: Original discretization and equivalent AIM grids for the geometry of Figure 8

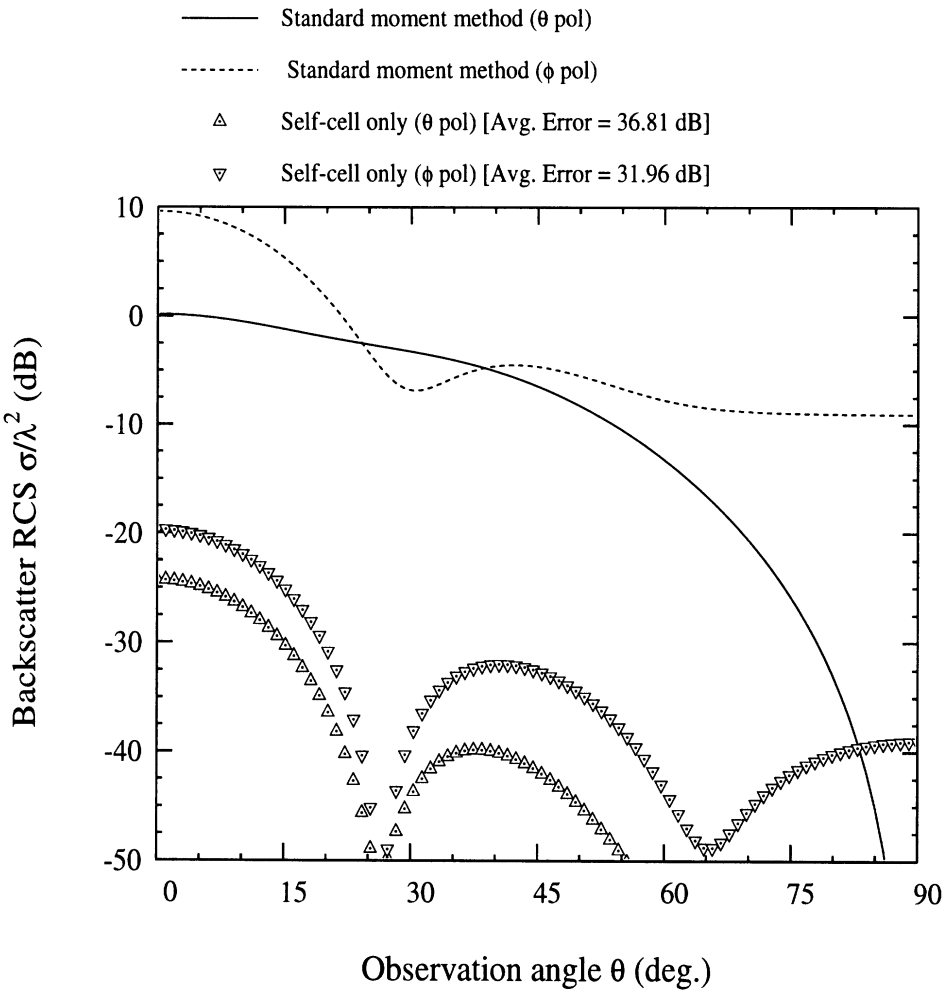

Figure 11: Error introduced by retaining only the self-cell interactions of the moment method

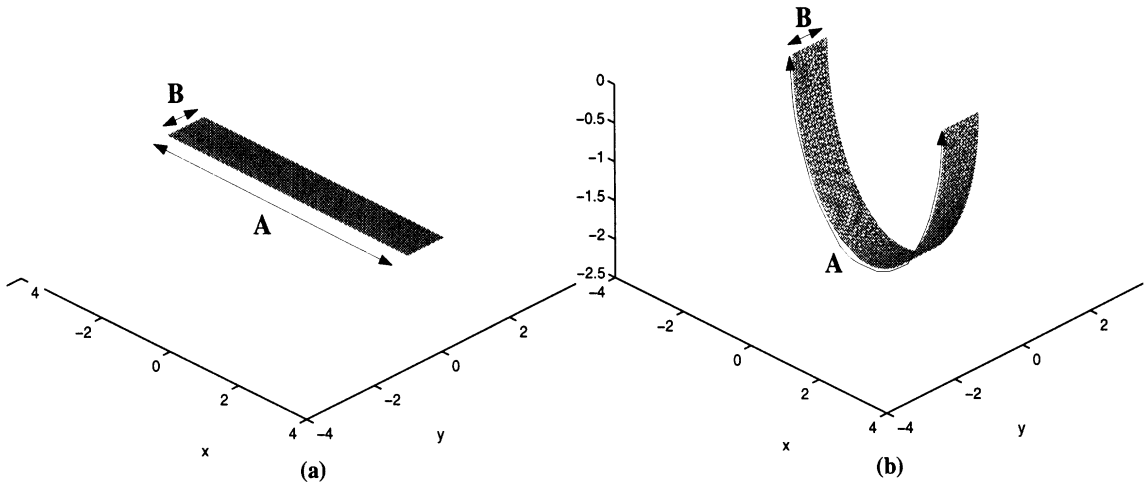

Figure 12: (a) Flat and (b) Curved plate with equal side lengths and discretization rates, resulting in equal number of unknowns. While the moment method yields equal solution time for both geometries, AIM would accelerate the solution for the geometry in (a) considerably more than that for the geometry in (b)

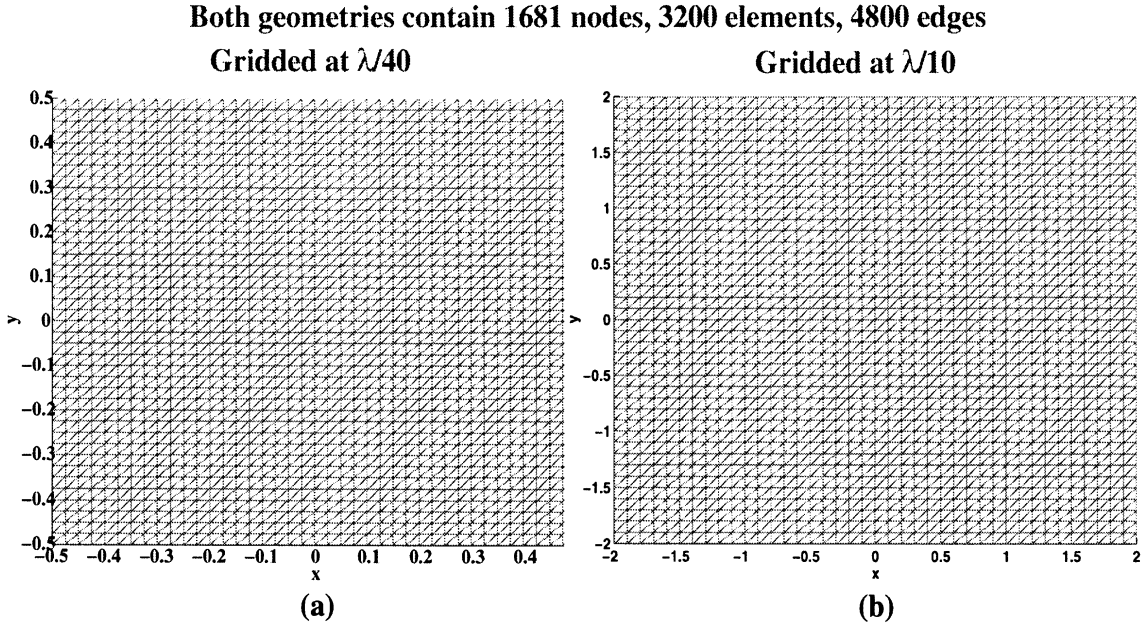

Figure 13: (a) Geometry of a 1λ square plate gridded at $\lambda/40$ and (b) 4λ square plate gridded at $\lambda/10$. While the moment method results in equal solution times for both geometries since they have equal number of unknowns, AIM would accelerate the solution for the geometry in (a) considerably more than that for the geometry in (b) owing to the smaller FFT pad for the geometry in (a)

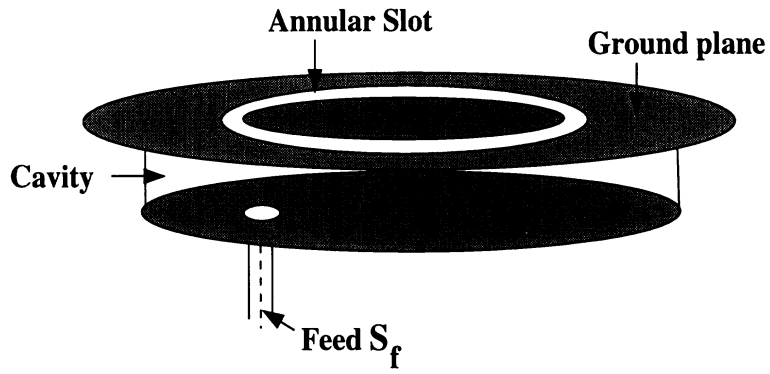

Figure 14: Geometry of a cavity-backed annular slot antenna in a ground plane

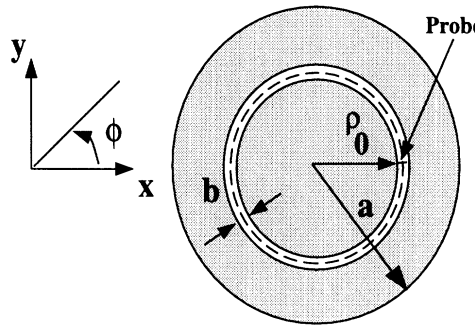

a = 12.35 cm
b = 0.75 cm
ρ_0 = 7.7 cm
Frequency = 1 GHz

	Non-zeros in near Z matrix
FE-BI	4656
FE-AIM (0.53 λ)	4656
FE-AIM (0.35 λ)	2245
FE-AIM (0.25 λ)	1537

	Average Error (dB)	
	Co-pol	X-pol
FE-AIM (0.35 λ)	0.4402	0.2998
FE-AIM (0.25 λ)	0.6343	0.5334

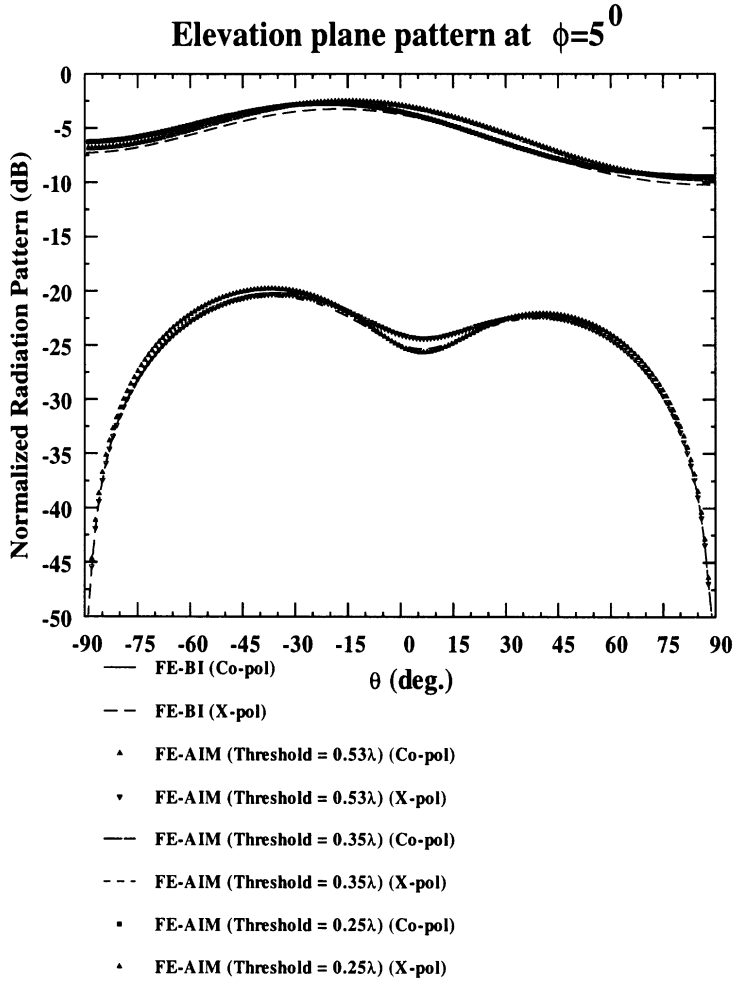

Figure 15: Radiation pattern from an annular slot in the $\phi = 0^0$ elevation plane

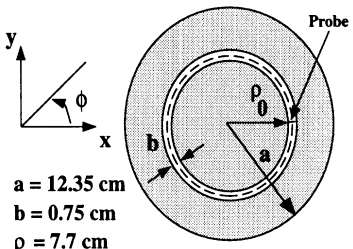

a = 12.35 cm
b = 0.75 cm
ρ_0 = 7.7 cm
Frequency = 1 GHz

	Non-zeros in near Z matrix
FE-BI	4656
FE-AIM (0.15 λ)	915
FE-AIM (0.25 λ)	1537
FE-AIM (0.35 λ)	2245

	Average Error (dB)	
	Co-pol	X-pol
FE-AIM (0.15 λ)	1.0524	1.0373
FE-AIM (0.25 λ)	0.6142	0.9105
FE-AIM (0.35 λ)	0.876	0.2506

(a)

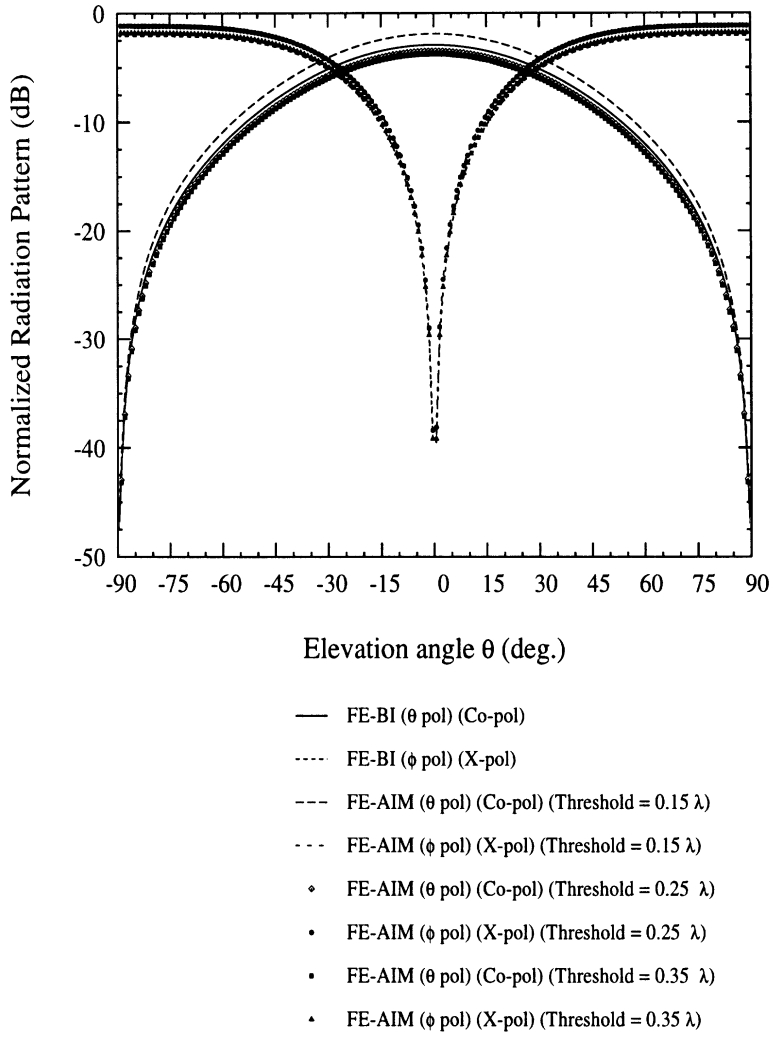

(b)

Figure 16: Radiation pattern from an annular slot in the $\phi = 90^0$ elevation plane

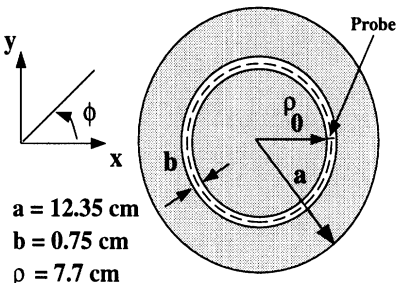

a = 12.35 cm
b = 0.75 cm
ρ_0 = 7.7 cm
Frequency = 0.73 GHz

	Non-zeros in near Z matrix
FE-BI	4656
FE-AIM (0.25 λ)	2184
FE-AIM (0.33 λ)	3272
FE-AIM (0.4 λ)	4656

	Average Error (dB) Co-pol
FE-AIM (0.25 λ)	1.3124
FE-AIM (0.33 λ)	1.0666
FE-AIM (0.4 λ)	0.00086

(a)

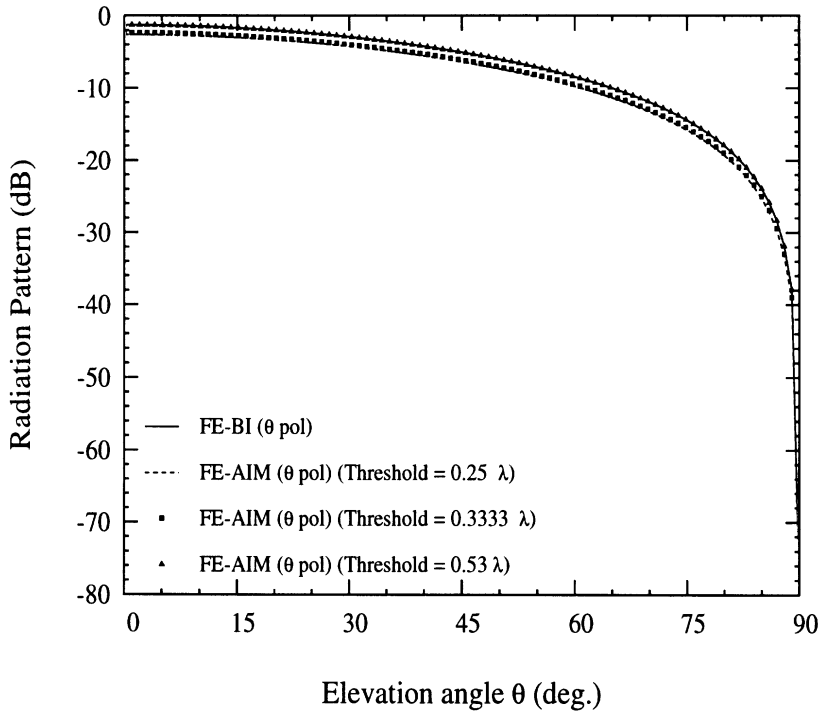

(b)

Figure 17: Bistatic scattering pattern from an annular slot; Normal incidence in the $\phi = 0^0$ plane and observation is in the $\phi = 90^0$ elevation plane

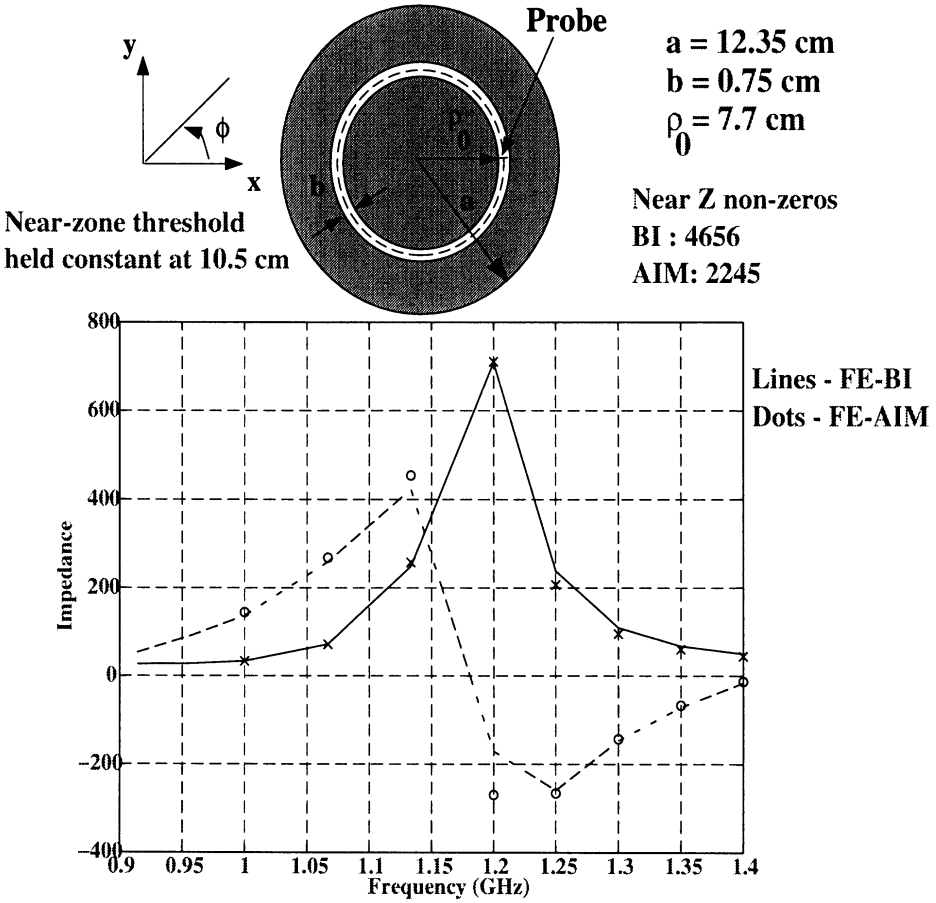

Frequency (GHz)	FE-BI	FE-AIM
1.0667	71.74 + j259.04	71.46 + j268.51
1.1333	248.51+j422.88	258.03 + j453.73
1.2	708.59-j170.31	710.39 - j269.71
1.25	238.47-j259.27	206.96 - j266.05
1.3	109.77-j146.96	95.48 - j142.82
1.35	67.63 - j71.61	59.84 - j 67.16
1.4	49.7 - j16.48	44.42-j12.95

Figure 18: Input impedance of a very narrow annular slot computed with FE-BI and FE-AIM

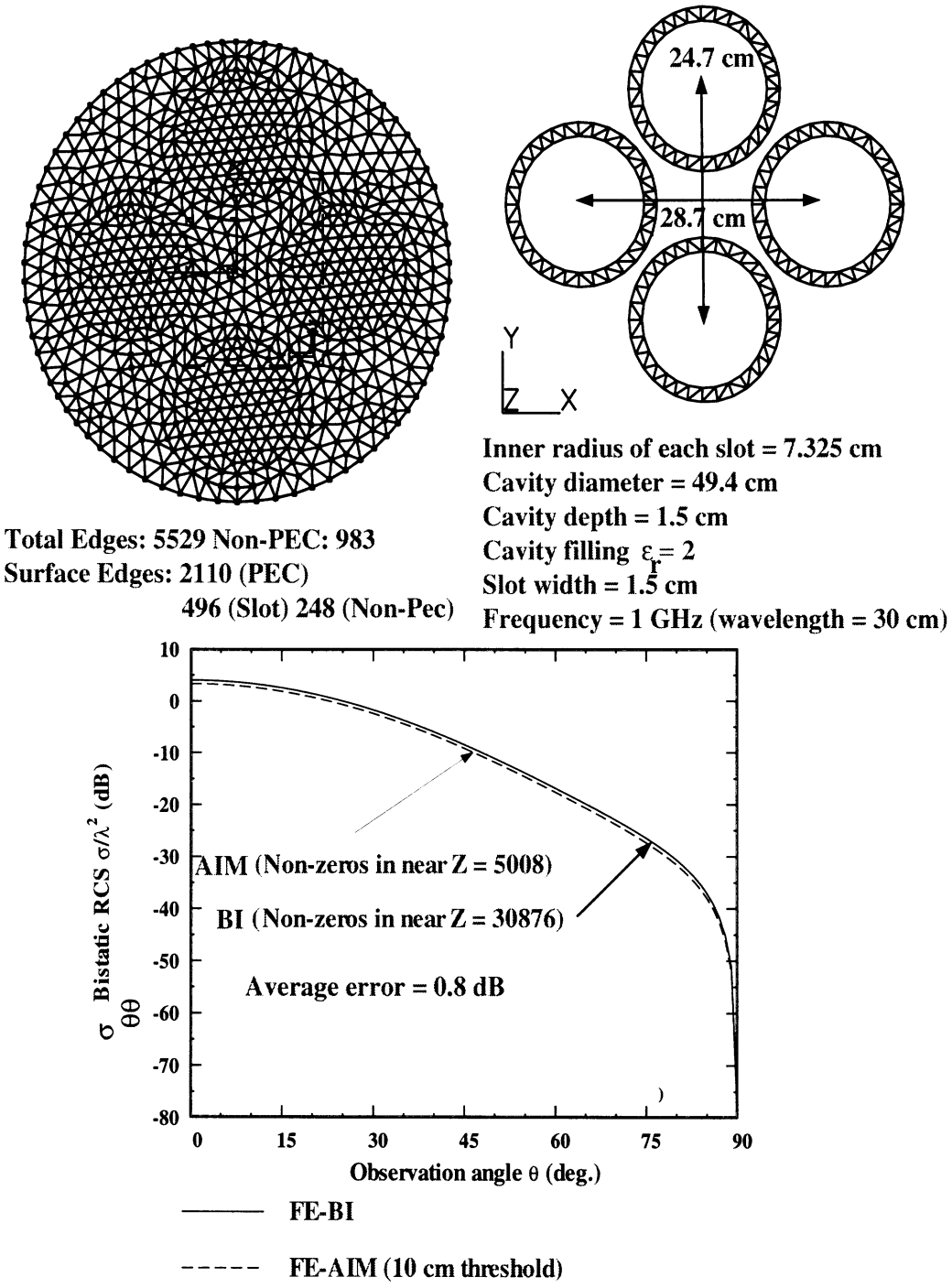

Figure 19: Bistatic RCS at normal incidence ($\phi = 90^0$ plane) from a cavity-backed slot array computed with FE-BI and FE-AIM

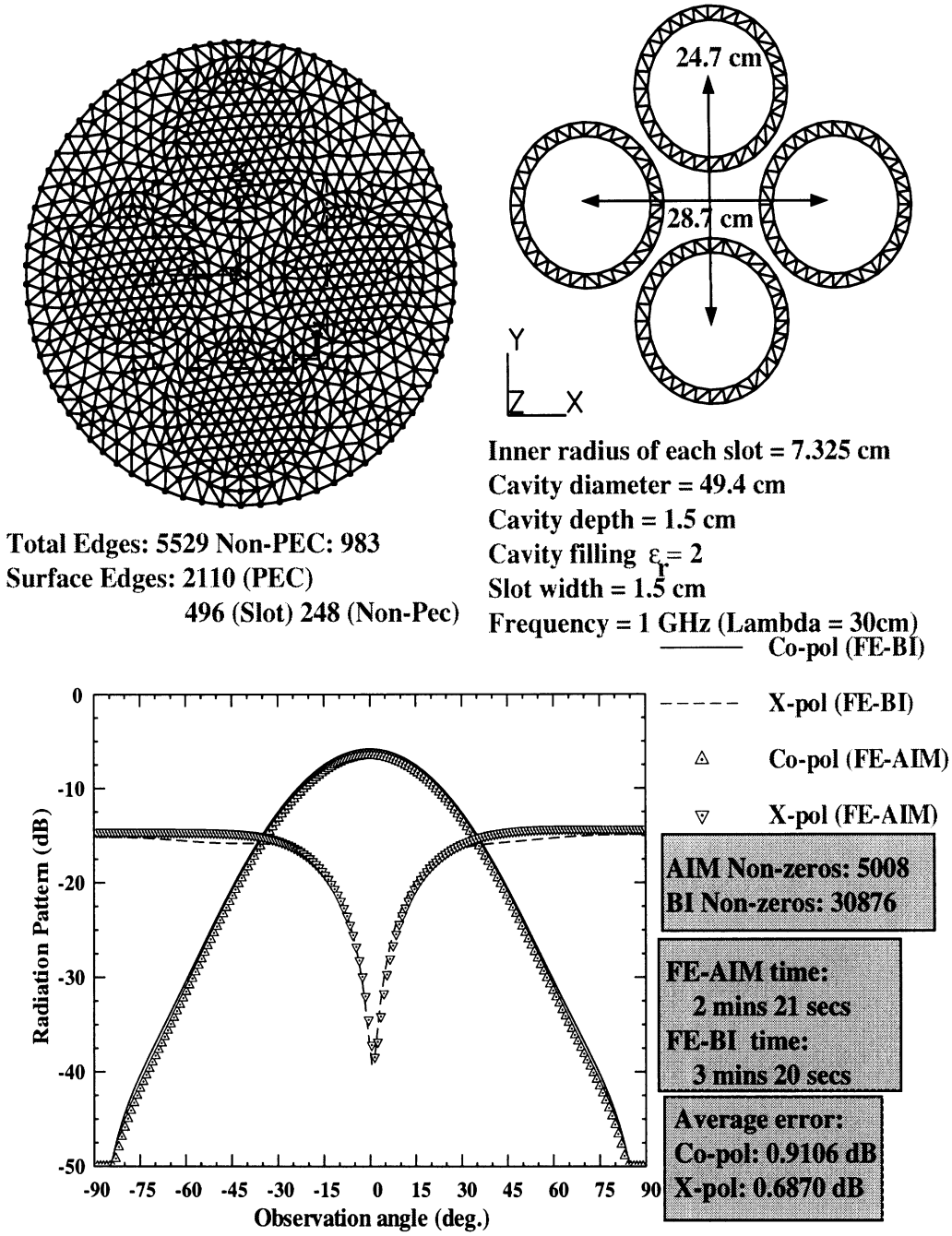

Figure 20: Radiation from a cavity-backed slot array computed with FE-BI and FE-AIM in the $\phi = 90^0$ plane

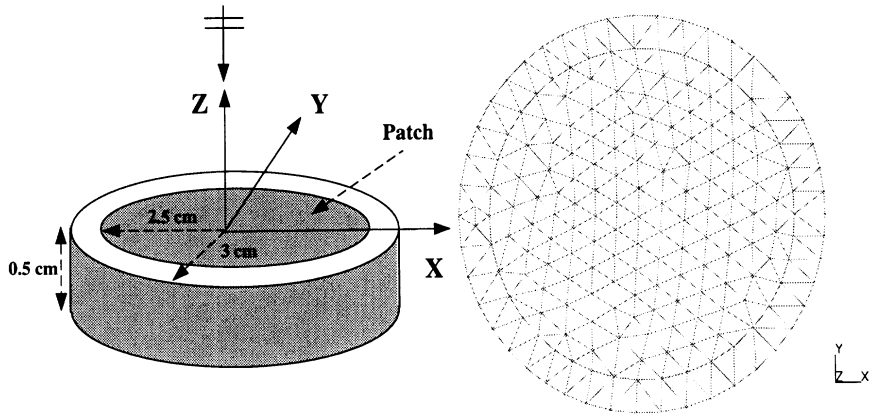

(a)

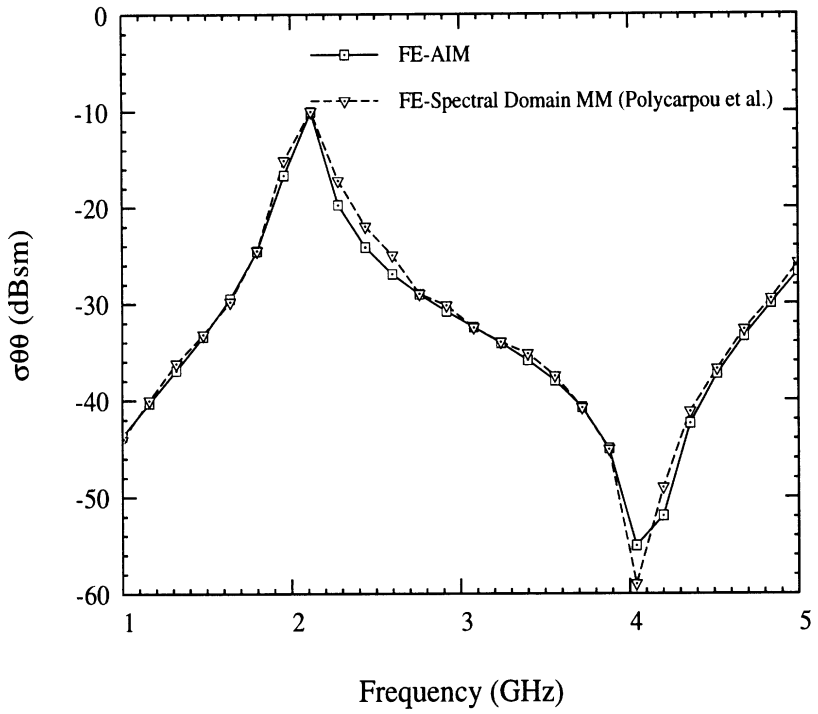

(b)

Figure 21: (a) Geometry and surface discretization of a cavity-backed patch antenna (b) Monostatic RCS at normal incidence versus frequency - cavity filling has a $\epsilon_r = 2.2 - j0.002$ and $\mu_r = 1$